Chemical Behavior and Local Structure of the Ruddlesden–Popper and Dion–Jacobson Alloyed Pb/Sn Bromide 2D Perovskites

Ping Fu, Michael Quintero, Eugenia Vasileiadou, Parth Raval, Claire Welton, Mikaël Kepenekian, George Volonakis, Jacky Even, Yukun Liu, Christos Malliakas, et al.

Chemical Behavior and Local Structure of the Ruddlesden−Popper and Dion−Jacobson Alloyed Pb/Sn Bromide 2D Perovskites

Ping Fu[#1,2] Michael A. Quintero[#2], Eugenia Vasileiadou[#2], Parth Raval,[3] Claire Welton,[3] Mikaël Kepenekian[4], George Volonakis[4], Jacky Even[5], Yukun Liu[6], Christos Malliakas[2], Yi Yang[2], Craig Laing[2], Vinayak P. Dravid[6], G. N. Manjunatha Reddy,[2,3] Can Li,[1] Edward H. Sargent[2] and Mercouri G. Kanatzidis[2*]

[1]*State Key Laboratory of Catalysis, Dalian Institute of Chemical Physics, Chinese Academy of Sciences, Dalian National Laboratory for Clean Energy, 457 Zhongshan Road, Dalian 116023, China*

[2]*Department of Chemistry, Northwestern University, Evanston, Illinois 60208, USA.*

[3]*University of Lille, CNRS, Centrale Lille, Univ. Artois, UMR 8181 – UCCS – Unité de Catalyse et Chimie du Solide, F-59000 Lille, France.*

[4]*Univ Rennes, ENSCR, INSA Rennes, CNRS, ISCR (Institute des Sciences Chimiques de Rennes), UMR 6226, France*

[5]*Univ Rennes, INSA Rennes, CNRS, Institute FOTON - UMR 6082, Rennes, France*

[6]*Department of Electrical and Computer Engineering, Northwestern University, Evanston, Illinois 60208, United States*

P. Fu, M. Quintero & E. Vasileiadou contribute equally to this work.

Corresponding Authors:

Mercouri G. Kanatzidis Email: m-kanatzidis@northwestern.edu

Abstract:

The alloyed lead/tin (Pb/Sn) halide perovskites have gained significant attention in the development of tandem solar cells and other optoelectronic devices due to their widely tunable absorption edge. To gain a better understanding of the intriguing properties of Pb/Sn perovskites, such as their anomalous bandgap dependence on stoichiometry, it is important to deepen the understanding of their chemical behavior and local structure. Herein, we investigate a series of two-dimensional Ruddlesden-Popper (RP) and Dion-Jacobson (DJ) phase alloyed Pb/Sn bromide perovskites using butylammonium (BA) and 3-(aminomethyl)pyridinium (3AMPY) spacer cations: $(BA)_2(MA)_{n-1}Pb_xSn_{n-x}Br_{3n+1}$ (n = 1−3) and $(3AMPY)(MA)_{n-1}Pb_xSn_{n-x}Br_{3n+1}$ (n = 1−3) through a solution-based approach. Our results show that the ratio and site preference of Pb/Sn atoms are influenced by the layer thickness (n) and spacer cations (A'), as determined by single crystal X-ray diffraction. Solid-state ^{1}H, ^{119}Sn and ^{207}Pb NMR spectroscopy analysis show that the Pb atoms prefer the outer layers in n=3 members: $(BA)_2(MA)Pb_xSn_{n-x}Br_{10}$ and $(3AMPY)_2(MA)Pb_xSn_{n-x}Br_{10}$. Layered 2D DJ alloyed Pb/Sn bromide perovskites: $(3AMPY)(MA)_{n-1}Pb_xSn_{n-x}Br_{3n+1}$ (n = 1−3) demonstrate much narrower optical band gap, higher energy PL emission and longer carrier lifetime compared to those of RP analogs. Density functional theory calculations suggest that Pb-rich alloys (Pb:Sn ~4) for n=1 compounds are thermodynamically favored over 50:50 (Pb:Sn ~1) compositions. From Grazing-Incidence Wide-Angle X-ray Scattering (GIWAXS), we see that films in the RP phase orient parallel to the substrate; whereas for DJ cases, random orientations are observed relative to the substrate.

Keyword: Halide perovskites; Lead/Tin bromide perovskites; Tandem solar cells, light emitting diodes

TOC Graphic

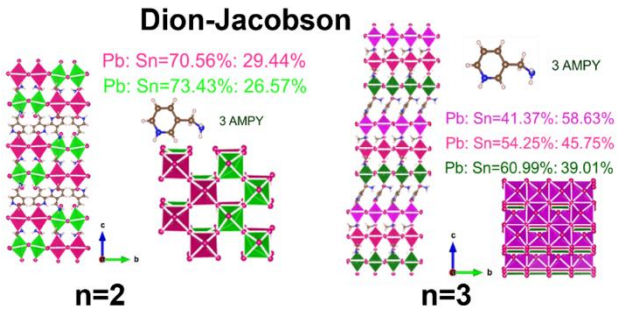

1. Introduction

The exceptional optoelectronic properties and performances of halide perovskites are driving a revolution in the photovoltaic and optoelectronic fields.[1-14] Organic-inorganic hybrid perovskites are three-dimensional (3D) with a prototypical formula of AMX_3 (A= methylammonium (MA), formamidinium, or Cs^+; M = Sn^{2+} or Pb^{2+}; X = Cl^-, Br^-, or I^-). The inorganic framework consists of corner-sharing octahedral $[MX_6]^{4-}$ units, where the small A-site cations occupy cuboctahedral cages within the framework and counterbalance the charge. This corner-sharing connectivity is responsible for their outstanding properties.[15] When larger spacer cations are incorporated, the two-dimensional (2D) perovskites can be obtained by splitting along different crystallographic planes, with the general formula of $(A')_m(A)_{n-1}M_nX_{3n+1}$, in which n is the thickness of inorganic layers, A′ is a monovalent (m = 2) cation forming the Ruddlesden−Popper (RP) phase[16-18] or divalent (m = 1) cation forming Dion-Jacobson (DJ)-phase,[19-22] respectively. Compared to the 3D perovskites, 2D analogues exhibit higher stability[23-28] and structural flexibility that permit a wider compositional space to engineer new materials, enhancing their potential for technological applications.[29]

Lately, numerous studies have examined the single-crystal structures of layered perovskites based on 2D pure lead iodide,[20, 30-32] pure lead bromide,[33-35] and pure tin halides .[36-40] It is well known that fully tin halide perovskites show poor stability due to the oxidation of Sn^{2+} to Sn^{4+} in the air. To address this issue, previous researches reported that adding a minimum content of Pb could stabilize Sn in its 2+ state in their

3D perovskite materials.[41, 42] These Pb/Sn systems have gained attention not only due to their reduced Pb content, which is considered harmful, but also because of their enhanced structural stability. Moreover, the band gap of the perovskite absorber can be adjusted through the Pb/Sn ratio in an unusual way, making them a promising option for lower band gap compounds in tandem solar cells and other optoelectronic applications.[6, 34, 41, 43-53]

However, the exploration of 2D alloyed Pb/Sn bromide analogues is relatively limited, and a comprehensive analysis of the structure-property relationship of this new family of 2D metal alloyed perovskite materials in bulk is currently lacking. These observations give rise to several questions: Can the Pb/Sn bromide perovskite serve as a template for the 2D RP and DJ phases? What is the conformation, Pb/Sn ratio, and site preference for Pb/Sn compounds with different cations? How does the DJ and RP single crystal materials determine the film orientation? These questions motivate the examination of narrow band-gap 2D alloyed Pb/Sn perovskite materials to investigate their fundamental structural and optoelectronic properties.

This study describes the synthesis, crystallographic and solid-state (ss)NMR analysis of a new array of 2D alloyed Pb/Sn bromide perovskite materials using monovalent butylammonium (BA^+) and divalent 3-(aminomethyl)pyridinium ($3AMPY^{2+}$) as spacer cations, the Ruddlesden-Popper $(BA)_2(MA)_{n-1}Pb_xSn_{n-x}Br_{3n+1}$ (n = 1−3) and the Dion-Jacobson $(3AMPY)(MA)_{n-1}Pb_xSn_{n-x}Br_{3n+1}$ (n = 1−3). Within the 2D perovskite structure, various families of alloyed Pb/Sn bromide perovskite single crystals (n=1-3) were stabilized. The optical properties, bandgaps and carrier lifetime were strongly affected by subtle structural differences among these perovskites. Layered 2D DJ alloyed Pb/Sn bromide perovskites: $(3AMPY)(MA)_{n-1}Pb_xSn_{n-x}Br_{3n+1}$ (n = 1−3) demonstrate much narrower optical band gap, higher energies PL emission and longer carrier lifetime compared to those of RP analogs. For both BA and 3AMPY (n=3) systems, the ^{207}Pb ssNMR signals associated with the outer layer are more intense than the inner layers, indicating that the Pb atoms are highly populated at the outer parts of the layers. Density functional theory calculations suggest that the Pb-rich alloys (Pb:Sn ~4) for n=1 compounds are thermodynamically preferred over 50:50 ratios that could

not be obtained experimentally. Successful production of thin films using these materials can be achieved through solution processing. The GIWAXS analysis indicates that the film orientation behavior of the RP and DJ phases exhibit noticeable divergence, which can serve as a valuable reference for developing optoelectronic devices utilizing these materials.

2. Results and discussion

2.1 Syntheses

The new family of compounds was synthesized using step-cooling method.[35] Briefly, a stoichiometric ratio of (molar ratio of PbO, $SnCl_2 \bullet 2H_2O$ 1:1) and MACl according to the chemical formula is used, where the concentration of the organic spacer is varied until a solution of pure product is obtained with the desired *n* value (e.g. n = 1-3). The solubility limit for $MAPbBr_3$ in HBr solution is ~0.56 M at boiling point, and the $Pb^{2+}/Sn^{2+}/MA^{+}$ concentration needs to be adjusted to it, while the HBr volume must be large enough to dissolve the *n*= 1 compound. Specifically, for the same stoichiometric amount of $Pb^{2+}/Sn^{2+}/MA^{+}$ (1:1:1 mmol) used, the amount of the large spacer cations, BA and 3AMPY needed to be tuned, then the synthetic procedure can be optimized to give different layer-numbers (n = 1−3).

Furthermore, an important parameter controlling the synthetic outcome of a uniform phase product with 3AMPY is the temperature cooling profile. If the reaction solutions are left to freely cool at room temperature (R.T.), a mixture of different numbers of inorganic layers (*n*) is usually obtained. This is vividly apparent in the cases of 3AMPY series, where *n*= 1 product is always obtained unless the reaction is cooled carefully and stepwise, over multiple days in the sand bath. Additionally, the quality and morphology of the crystals are significantly improved with stepwise cooling temperature profiles in the sand bath, where less crystallographic twinning is observed. Accordingly, after the subsequent addition of all the reagents together and once a clear solution is formed, the temperature is lowered to slightly below the boiling point of HBr to 120 °C (as indicated on a hot plate). The solution is held at this temperature for several days under reflux to avoid the formation of other *n*-layer members. Once the light-yellow crystal seeding starts, the temperature of the reaction solution is lowered to 95 °C (as indicated on a hot plate) and left for a couple of days for crystal growth. Finally, the hot plate is turned off for full crystal precipitation to be achieved. The

crystals are dried from the reaction solution by careful vacuum filtration, the crystals are left under vacuum in a desiccator overnight. Upon drying, the bulk crystals exhibit excellent stability in ambient conditions. The powder X-ray diffraction (PXRD) patterns of $(BA)_2(MA)_{n-1}Pb_xSn_{n-x}Br_{3n+1}$ (n = 1−3, x=0.83-2.02) and $(3AMPY)(MA)_{n-1}Pb_xSn_{n-x}Br_{3n+1}$ (n = 1−3, x=0.79-1.56) as shown in **Figure 1,** especially for the higher angles between 5° and 15°, indicating the reasonably good long-range order.[54] The d-spacing of the first Bragg peak in the PXRD pattern is a characteristic peak for each n member compound, corresponding to the length of the stacking axis in the unit cell of the respective 2D perovskite member, thus providing an easy assessment of the n member compound acquired.

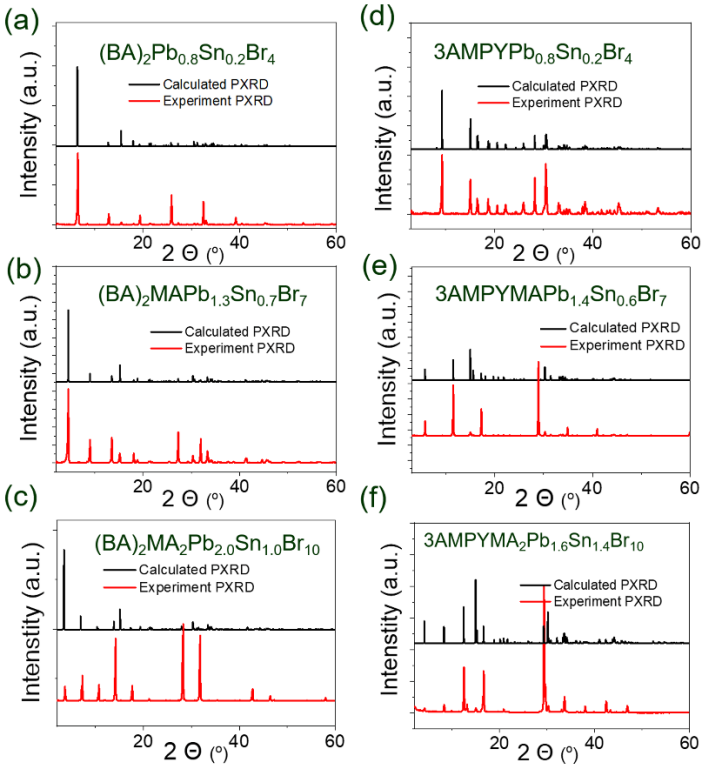

Figure 1. Calculated and experimental powder X-ray diffraction (PXRD) patterns for (a-c) (BA) $(MA)_{n-1}Pb_xSn_{n-x}Br_{3n+1}$ and (d-f) $(3AMPY)(MA)_{n-1}Pb_xSn_{n-x}Br_{3n+1}$ (n = 1−3) series powder compounds, respectively.

According to the scanning electron microscopy (SEM) mapping studies, the newly developed compounds are extremely thin and can be easily stacked on top of each other, as depicted in **Figure 2.** The unique feature of the 2D multi-layered crystal structure is the plate-like shape of the individual crystals and the layered morphology resulting from stacking.[35] The sizes of bulk crystals are in the range of several um~ mm. Minor cracks on the single crystal surfaces do exist, but majority of the bulk form of the large

crystals still retains the form of layered 2D single crystals that are stacked on top of each other. The energy dispersive spectrometry (EDS) mapping confirms that the Pb and Sn elements in the multilayer (n>1) halide perovskites are evenly distributed (n>1) halide perovskites are evenly distributed. The compounds exhibit a color change as the value of n increases from 1 to 3. In the RP phase $(BA)_2(MA)_{n-1}Pb_xSn_{n-x}Br_{3n+1}$ series, the color changes from yellow (n=1) to orange (n=2), while in the DJ phase $(3AMPY)_2(MA)_{n-1}Pb_xSn_{n-x}Br_{3n+1}$ series, it changes from orange (n=1) to red (n=2).

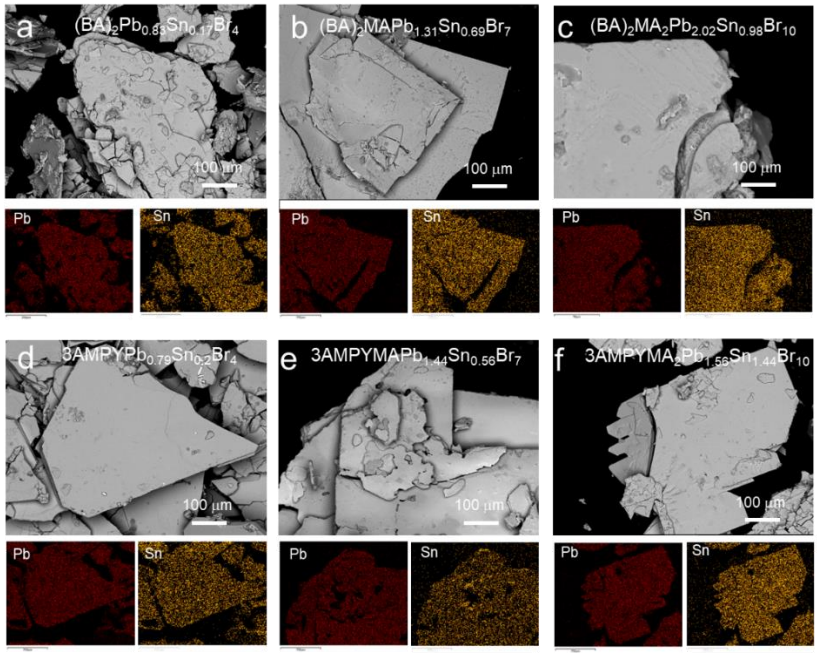

Figure 2. Overall microstructure and composition analyses: Scanning Electron Microscopy/Energy Dispersive X-ray Spectrometry (SEM/EDS) of (a-c) $(BA)_2(MA)_{n-1}Pb_xSn_{n-x}Br_{3n+1}$ (n = 1−3) and (d-f) (3AMPY) $(MA)_{n-1}Pb_xSn_{n-x}Br_{3n+1}$ (n = 1−3) series powder compounds, respectively.

2.2 Description of the Crystal Structures

For the optimal utilization of the optoelectronic properties of 2D alloyed Pb/Sn perovskites, it is important to possess accurate structural information of each compound to develop the structure-property relationships. The crystal structures of all the compounds under investigation were determined by utilizing data from single crystal X-ray diffraction (SCXRD) that were collected at room temperature. Selected crystallographic information and structural refinements for the $(BA)_2(MA)_{n-1}Pb_xSn_{n-x}Br_{3n+1}$ and $(3AMPY)(MA)_{n-1}Pb_xSn_{n-x}Br_{3n+1}$ (n = 1−3) series are presented in **Table 1**.

Detailed crystallographic data are also provided in **Tables S1−S4**. Specifically, the studied 2D perovskites consist of corner-sharing $[Sn_{1-x}Pb_xBr_6]^{-4}$ octahedra and the metal sites are occupied by both Sn and Pb atoms. The distribution is not totally random as there are specific preferences of Pb and Sn for particular crystallographic sites, as discussed below. The $(BA)_2(MA)_{n-1}Pb_xSn_{n-x}Br_{3n+1}$ series forms the Ruddlesden−Popper (RP) structure type with staggered configuration of the successive inorganic layers and the $(3AMPY)(MA)_{n-1}Pb_xSn_{n-x}Br_{3n+1}$ (n = 1−3) series forms the Dion-Jacobson (DJ) structure type with eclipsed configuration of the successive inorganic layers, respectively.[19, 55-57]

Table 1. Crystal data and structure refinement for $(BA)_2(MA)_{n-1}Pb_xSn_{n-x}Br_{3n+1}$ (n = 1−3) and $(3AMPY)(MA)_{n-1}Pb_xSn_{n-x}Br_{3n+1}$ (n = 1−3) at 293 K.

Compound	$(BA)_2Pb_{0.83}Sn_{0.17}Br_4$	$(BA)_2MAPb_{1.31}Sn_{0.69}Br_7$	$(BA)_2MA_2Pb_{2.02}Sn_{0.98}Br_{10}$
Empirical formula	C8H20Br4N2Pb0.83Sn0.17	C9H25Br7N3Pb1.31Sn0.69	C10H36Br10N4Pb2.02Sn0.98
Formula weight	656.49	1088.00	1546.14
Crystal system	orthorhombic	orthorhombic	orthorhombic
Space group	Cmc21	Pbcn	Cmc21
Unit cell dimensions	a = 27.641(6) Å, α = 90° b = 8.3381(17) Å, β = 90° c = 8.2230(16) Å, γ = 90°	a = 39.1754(17) Å, α = 90° b = 8.3831(3) Å, β = 90° c = 8.2683(3) Å, γ = 90°	a = 51.082(3) Å, α = 90° b = 8.3679(4) Å, β = 90° c = 8.2930(4) Å, γ = 90°
Volume	1895.2(7) $Å^3$	2715.40(18) $Å^3$	3544.8(3) $Å^3$
Z	4	4	4
Density (calculated)	2.301 g/cm^3	2.661 g/cm^3	2.897 g/cm^3
Absorption coefficient	16.070 mm^{-1}	10.232 mm^{-1}	21.524 mm^{-1}
Index ranges	-38<=h<=38, -11<=k<=11, -11<=l<=10	-58<=h<=58, -12<=k<=12, -11<=l<=12	-72<=h<=77, -12<=k<=11, -12<=l<=10
Reflections collected	7243	20923	19722
Independent reflections	2566 [R_{int} = 0.0424]	4833 [R_{int} = 0.0352]	5729 [R_{int} = 0.0387]
Completeness	99.8%	98.5%	99.9%
Data / restraints / parameters	2566 / 22 / 77	4833 / 34 / 102	5729 / 30 / 116
Goodness-of-fit	1.050	1.130	1.032

Final R indices [I > 2σ(I)]	R_{obs} = 0.0586, wR_{obs} = 0.1588	R_{obs} = 0.0900, wR_{obs} = 0.2158	R_{obs} = 0.0479, wR_{obs} = 0.1098
R indices [all data]	R_{all} = 0.0838, wR_{all} = 0.1799	R_{all} = 0.1203, wR_{all} = 0.2336	R_{all} = 0.0799, wR_{all} = 0.1216
Largest diff. peak and hole	2.459 and -3.228 e·Å^{-3}	1.650 and -2.226 e·Å^{-3}	2.263 and -0.843 e·Å^{-3}
Compound	(3AMP)$Pb_{0.79}Sn_{0.21}Br_4$	(3AMP)$MAPb_{1.44}Sn_{0.56}Br_7$	(3AMP)$MA_2Pb_{1.56}Sn_{1.44}Br_{10}$
Empirical formula	C6H10Br4N2Pb0.79 Sn0.21	C7H16Br7N3Pb1.44Sn0.56	C8 H22 Br10 N4 Pb1.56 Sn1.44
Formula weight	618.18	1066.42	1467.75
Crystal system	Triclinic	Monoclinic	Monoclinic
Space group	P $\bar{1}$	$P2_1/c$	Cc
Unit cell dimensions	a = 10.614(2) Å, α = 86.72(3)° b = 11.851(2) Å, β = 64.57(3)° c = 11.896(2) Å, γ = 81.14(3)°	a = 15.568(3) Å, α = 90° b = 17.165(3) Å, β = 97.23(3)° c = 8.2140(16) Å, γ = 90°	a = 42.906(9) Å, α = 90° b = 8.5286(17) Å, β = 95.82(3)° c = 8.2673(17) Å, γ = 90°
Volume	1335.2(6) Å^3	2177.5(8) Å^3	3009.6(11) Å^3
Z	4	4	4
Density (calculated)	3.075 g/cm^3	3.253 g/cm^3	3.239 g/cm^3
Absorption coefficient	11.984 mm^{-1}	13.223 mm^{-1}	12.439 mm^{-1}
Index ranges	-14<=h<=14, -15<=k<=16, -16<=l<=16	-19<=h<=19, -21<=k<=21, -10<=l<=10	-72<=h<=70, -14<=k<=13, -12<=l<=14
Reflections collected	25517	14407	18244
Independent reflections	7087 [R_{int} = 0.0312]	4561 [R_{int} = 0.0786]	9868 [R_{int} = 0.0813]
Completeness	99.6%	96.2%	99.6%
Data / restraints / parameters	7087 / 2 / 239	4561 / 5 / 132	9868 / 33 / 175
Goodness-of-fit	0.665	0.905	0.634
Final R indices [I > 2σ(I)]	R_{obs} = 0.0253, wR_{obs} = 0.0391	R_{obs} = 0.0660, wR_{obs} = 0.1713	R_{obs} = 0.0870, wR_{obs} = 0.2005
R indices [all data]	R_{all} = 0.0484, wR_{all} = 0.0403	R_{all} = 0.1083, wR_{all} = 0.1928	R_{all} = 0.2011, wR_{all} = 0.2170
Largest diff. peak and hole	1.697 and -0.880 e·Å^{-3}	4.175 and -2.329 e·Å^{-3}	11.722 and -2.398 e·Å^{-3}

$R = \Sigma||F_o|-|F_c|| / \Sigma|F_o|$, $wR = [\Sigma[w(|F_o|^2 - |F_c|^2)^2] / \Sigma[w(|F_o|^4)]]$

The $(BA)_2(MA)_{n-1}Pb_xSn_{n-x}Br_{3n+1}$ (n = 1-3) series crystallize in high symmetry orthorhombic space groups. The $(BA)_2Pb_{0.83}Sn_{0.17}Br_4$ (n=1) and $(BA)_2MA_2Pb_{2.02}Sn_{0.98}Br_{10}$ (n=3) members adopts the non-centrosymmetric space

groups ($Cmc2_1$), while $(BA)_2MAPb_{1.31}Sn_{0.69}Br_7$ (n=2) is centrosymmetric (*Pbcn*). The DJ phase $(3AMPY)(MA)_{n-1}Pb_xSn_{n-x}Br_{3n+1}$ (n = 1−2) series are in centrosymmetric space groups of $P\bar{1}$ (n=1, x=0.79) and $P2_1/c$ (n=2, x=1.56), while the $(3AMPY)MA_2Pb_{1.56}Sn_{1.44}Br_{10}$ (n = 3) exhibits a non-centrosymmetric *Cc* space group.

For $(BA)_2Pb_{0.83}Sn_{0.17}Br_4$ (n=1), there is only one kind of octahedron with 82.80% Pb occupancy (17.20 % Sn occupancy) and the ratio of Pb/Sn is almost 4.81 (**Figure 3a**). For the $(3AMPY)Pb_{0.79}Sn_{0.21}Br_4$ (n=1), adjacent organic cations adopt an edge-to-face interaction and they show two kinds of octahedra. One has 79.45% Pb occupancy (20.55% Sn occupancy), and the other one has 78.33% Pb occupancy (21.67% Sn occupancy). The final ratio of Pb/Sn is also almost 3.74 (**Figure 3b**).

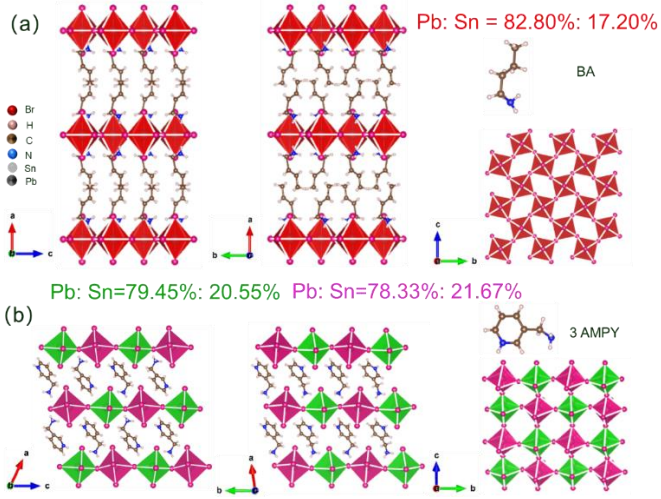

Figure 3. Comparative view of the crystal structures for (a) the $(BA)_2(Pb_{0.83}Sn_{0.17})Br_4$ (n = 1, x= 0.83) and (b) $(3AMPY)Pb_{0.79}Sn_{0.21}Br_4$ (n = 1, x= 0.79), respectively.

For $(BA)_2MAPb_{1.31}Sn_{0.69}Br_7$ (n=2), there is still only one kind of octahedron with 65.33% Pb occupancy and 34.67% Sn occupancy (**Figure 4a**). The ratio of Pb/Sn increased to 1.88. The length of the Br−Pb/Sn−Br unit is approximately 5.8 Å, which makes up the length of one $[Pb_xSn_{1-x}Br_6]^{4-}$ octahedron of the inorganic layer. Thus, the length of the stacking axis follows the formula of ~ 5.8n + y Å, where n is the layer-number and y is the distance between the inorganic layers.[35]

For $(3AMPY)(MA)Pb_{1.44}Sn_{0.56}Br_7$ (n=2), there are two kinds of octahedra, the one which is adjacent the edge of 3AMPY, has 73.43% Pb occupancy (26.57% Sn

occupancy), and the other one which is adjacent the face of 3AMPY, has 70.56% Pb occupancy (29.44% Sn occupancy). The final ratio of Pb/Sn in (3AMPY)(MA)$Pb_{1.44}Sn_{0.56}Br_7$ (n=2) is also larger compared to $(BA)_2MAPb_{1.31}Sn_{0.69}Br_7$ (n=2), up to a value of 2.58 (**Figure 4b**). In addition, the distances between stacked aromatic pyridinium rings for (3AMPY)(MA)$Pb_{1.44}Sn_{0.56}Br_7$ is 3.19 Å, falling within the range of π–π stacking interaction. Thus, the stacking direction of the aromatic pyridinium ring is highly ordered with the aromatic planes in the direction of the b axis.[58]

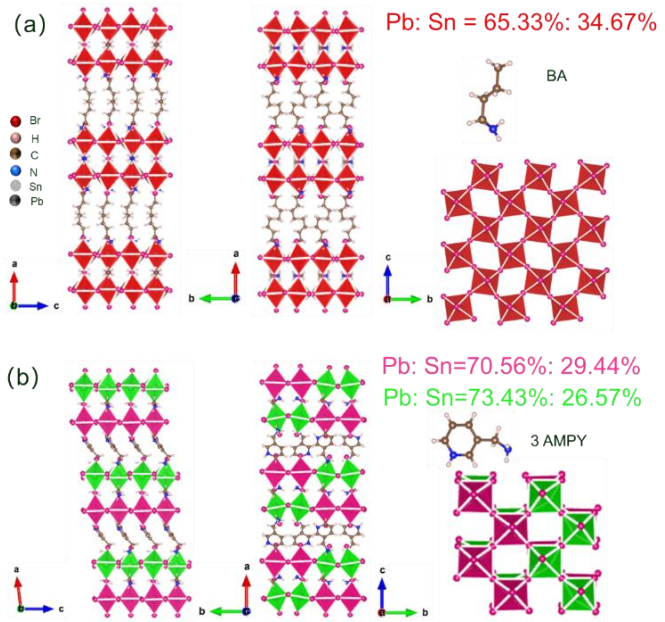

Figure 4. Comparative view of the crystal structures for (a) the $(BA)_2(MA)(Pb_{1.31}Sn_{0.69})_2Br_7$ (n = 2, x= 1.31) and (b) (3AMPY)(MA)$(Pb_{1.44}Sn_{0.56})_2Br_7$ (n = 2, x= 1.44), respectively.

For the n=3 $(BA)_2MA_2Pb_{2.02}Sn_{0.98}Br_{10}$ compounds, Pb may have some site preference in the material for the middle octahedral layer over the layers adjacent to the organic cations. The middle octahedra for $(BA)_2(MA)_2Pb_{2.02}Sn_{0.98}Br_{10}$ have 68.76% Pb occupancy (31.24% Sn occupancy) while the outer octahedra have 65.66% Pb occupancy (34.34% Sn occupancy) (**Figure 5a**). The final ratio of Pb/Sn is also almost 2.06. As a comparison, if we change the BA cations by increasing the length of carbon chain to heptylamine (HEP), the middle octahedra of $(HEP)_2(MA)_2Pb_{1.95}Sn_{1.05}Br_{10}$ have 72.36% Pb occupancy (27.64% Sn occupancy) and the outer octahedra have 56.20% Pb occupancy (43.80% Sn occupancy). The final ratio of Pb/Sn is also almost 1.95

(**Figure S1 and Table.S5**). For (3AMPY)$MA_2Pb_{1.56}Sn_{1.44}Br_{10,}$ there are three kinds of octahedra, the middle one has 54.25% Pb occupancy (45.75% Sn occupancy), and the outer two have 60.99% Pb occupancy (39.01% Sn occupancy) and 41.37% Pb occupancy (58.63% Sn occupancy), respectively. The final ratio of Pb/Sn is also increased, up to a value of 1.08 (**Figure 5b**). It is evident that the choice of the cations and the layer numbers show an influence on the site preference of Pb and Sn. All the Pb and Sn occupancies are consistent with the results from EDS mapping images (**Figure 2** and **Table.S6**).

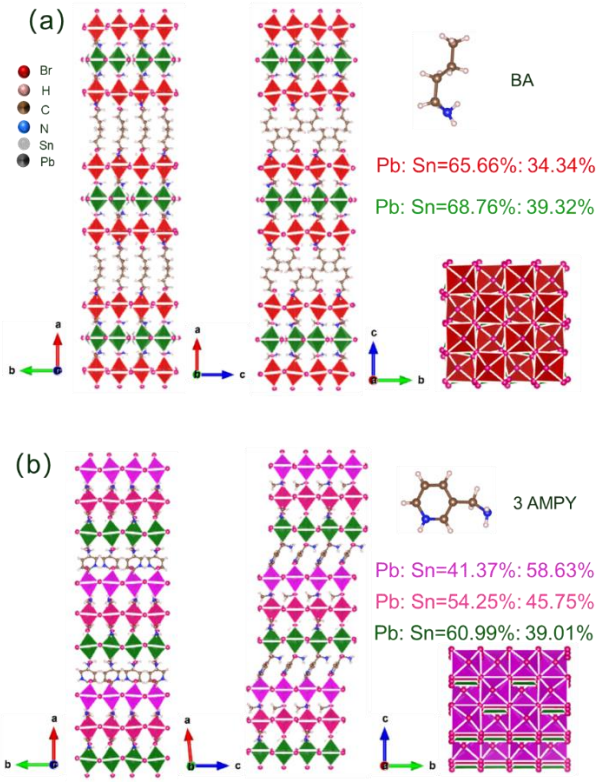

Figure 5. Comparative view of the crystal structures for (a) the $(BA)_2(MA)_2(Pb_{2.02}Sn_{0.98})_3Br_{10}$ (n = 3, x= 2.02) and (b) $(3AMPY)(MA)_2(Pb_{1.56}Sn_{1.44})_3Br_{10}$ (n = 3, x= 1.56), respectively.

It is worthy to draw comparison to the pure Pb and pure Sn 2D perovskite analogs with the same cations as listed in **Table 2.** With BA cations, a pure Pb-based RP material $(BA)_2PbBr_4$ (n=1) can crystallize with the Pbca space group, but with pure Sn, it can form into 0D structure $(BA)_2SnBr_6$ with $P2_1$ space group and 2D structure $(BA)_2SnBr_4$

with *P*1 space group (**Figure S2 and Table 2**). For 3AMPY cations, a Sn-based 2D DJ n=1 phase 3AMPYSnBr$_4$ is formed with the *P*1 space group, but with pure Pb, only a 0D structure is obtained with the Pbca space group (**Figure S2 and Table 2**). Moreover, the mixed Pb/Sn perovskite bromide compounds with BA and 3AMPY cations (n=1): $(BA)_2Pb_{0.83}Sn_{0.17}Br_4$ and $(3AMPY)Pb_{0.79}Sn_{0.21}Br_4$, can form both 2D crystallographic structures, but those are different than the ones of pure $(BA)_2PbBr_4$ and 3AMPYSnBr$_4$, indicating that Pb/Sn alloying has a strong impact on the structural properties. Pb/Sn alloying has less effect on the space group as the layer number increases, as the same Cmc21 space groups is retrieved for n=3 pure Pb, pure Sn and Pb/Sn compounds with BA cations. The different sizes of Pb and Sn atoms results in the unit cell volumes in descending order, related to pure Pb compounds > Pb/Sn cases> pure Sn cases. The structural details of the inorganic layer can be significantly influenced by the type of organic spacers due to their soft and flexible nature. In the case of BA cations, they are interdigitated between the inorganic layers, allowing for the organic tail to move more freely.[59] The gap between the layers is filled by the relatively short 3AMPY cations in DJ phases, which stiffen the structure and bring the layers into closer proximity.[19] Consequently, the atoms of the cation experience restricted movement, and the distortion of the perovskite octahedra may differ from that observed in the RP cases.

Table 2. Crystal data comparison for $(BA)_2(MA)_{n-1}Pb_xSn_{n-x}Br_{3n+1}$ (n = 1−3), pure lead $(BA)_2$ $(MA)_{n-1}Pb_nBr_{3n+1}$ (n = 1−3) and pure tin $(BA)_2$ $(MA)_{n-1}Sn_nBr_{3n+1}$ (n = 1−3) compounds.

Compound	Structure	Space group	Unit cell		V (Å^3)	Bond Angle variance (deg^2)	Bond length distortion
$(BA)_2PbBr_4$[60]	2D (n=1)	Pbca	a = 8.25460 Å b = 8.14220 Å c = 27.46310 Å	α = 90° β = 90° γ = 90°	1845.8116	8.5419	0.00509
$(BA)_2Pb_{0.83}Sn_{0.17}Br_4$ This work	2D (n=1)	Cmc21	a = 27.641(6) Å, b = 8.3381(17) Å, c = 8.2230(16) Å,	α = 90° β = 90° γ = 90°	1895.2(7)	0.3401	0.0041

$(BA)_2SnBr_6$	0D	P 21	a = 10.34200 Å b = 7.67800 Å c = 12.51700 Å	α = 90° β = 103.23° γ = 90°	967.5438	1.3323	0.00467
$(BA)_2MAPb_2Br_7$[61]	2D (n=2)	Cmc21	a = 39.13580 Å b = 8.34630 Å c = 8.18040 Å	α = 90° β = 90° γ = 90°	2672.0387	20.1010	0.01070
$(BA)_2MAPb_{1.31}Sn_{0.69}Br_7$ This work	2D (n=2)	Pbcn	a = 39.1754(17) Å, b = 8.3831(3) Å, c = 8.2683(3) Å,	α = 90° β = 90° γ = 90°	2715.40(18)	9.7383	0.0131
$(BA)_2MA_2Pb_3Br_{10}$[62]	2D (n=3)	Cmc21	a = 51.02100 Å b = 8.37830 Å c = 8.28740 Å	α = 90° β = 90° γ = 90°	3608.9314	1.5038	0.00762
$(BA)_2MA_2Pb_{2.02}Sn_{0.98}Br_{10}$ This work	2D (n=3)	Cmc21	a = 51.082(3) Å, b = 8.3679(4) Å, c = 8.2930(4) Å,	α = 90° β = 90° γ = 90°	3544.8(3)	12.7891	0.0188
$(BA)_2MA_2Sn_3Br_{10}$[36]	2D (n=3)	Cmc21	a = 51.02100 Å b = 8.37830 Å c = 8.28740 Å	α = 90° β = 90° γ = 90°	3542.6086	14.3106	0.02546
$(3AMPY)PbBr_6$[63]	0D	Pbca	a = 15.78800 Å b = 8.14600 Å c = 17.21500 Å	α = 90° β = 90° γ = 90°	2214.0048	5.2751	0.00463
$(3AMPY)Pb_{0.79}Sn_{0.21}Br_4$ This work	2D (n=1)	P $\bar{1}$	a = 10.614(2) Å, b = 11.851(2) Å, c = 11.896(2) Å,	α = 86.72(3)° β = 64.57(3)° γ = 81.14(3)°	1335.2(6)	35.907	0.0115
$(3AMPY)SnBr_4$ This work	2D (n=1)	P 1	a = 10.717(2) Å, b = 11.811(2) Å, c = 11.833(2) Å,	α = 85.04(3)° β = 63.76(3)° γ = 80.94(3)°	1326.45(6)	34.762	0.0465

In the ideal 2D perovskite tetragonal structure, the four closest metal atoms within a plane shape a square, and the octahedra are untitled (i.e., the Pb-Br-Pb angles are equal to 180°). However, for the tilted structures, two opposite edges of the square are "pulled-in" while the other two are "pushed-out." To gain an understanding of these distortions in the tilted structures, the mean distortion level of each octahedron is calculated for each compound. The mean bond length distortion, (Δd) is defined by $\Delta d = \left(\frac{1}{6}\right)\sum[\frac{|d_n - d|}{d}]$, where d is the average Pb−Br bond distance and d_n represent the six individual bond distances.[64, 65] The distortion of the perovskite lattice can also be characterized by the bond angle variance (σ) calculated by the expression $\sigma^2 = \sum_1^{12} i(\theta_i$

$- 90)^2/11$, where θ_i is the individual Br−Pb−Br bond angle.[66] The BA and 3AMPY series are modeled with restraints of bond lengths and angles, which is nicely reflected in the refinement statistics as listed in **Table 3**. For 2D RP phase perovskite structures, the mean bond angle variance and bond length distortion are in descending order, related to $(BA)_2(MA)_2Pb_{2.02}Sn_{0.98}Br_{10}$ > $(BA)_2MAPb_{1.31}Sn_{0.69}Br_7$ > $(BA)_2Pb_{0.83}Sn_{0.17}Br_4$. Thus, as the layer-number increases, the distortion for the $(BA)_2(MA)_{n-1}Pb_xSn_{n-x}Br_{3n+1}$ series becomes larger. On the contrary, in the $(3AMPY)(MA)_{n-1}Pb_xSn_{n-x}Br_{3n+1}$ series, the mean bond length distortion also increases with n while the mean bond angle variance decreases. It is well known that the distortion levels of the inorganic octahedra assessed through the bridging Pb−Br−Pb angles are correlated with the bandgap of the materials. In order to compare the RP and DJ phases (n=2, 3), we classify the Pb−Br−Pb angles into two categories, the equatorial angle (parallel to the inorganic plane) and the axial angle (in the stacking direction). The BA series (n=2) is distorted mainly in-plane (equatorial Pb/Sn−Br−Pb/Sn angle 163.09°) and barely distorted out-of-plane (axial Pb/Sn−Br−Pb/Sn angle 179.93°). The 3AMPY (n=2) is distorted both in-plane and out-of-plane (equatorial Pb/Sn−Br−Pb/Sn angle 167.49° and axial Pb/Sn−Br−Pb/Sn angle 170.02°). The rigidity of the aromatic system restricts the ring to planarity, so the inorganic layers are slightly staggered to accommodate the asymmetry of the 3AMPY cation. Thus, 3AMPY series (n=2) shows a larger bond angle variance, but a bit smaller bond length distortion compared to the BA series (n=2), which might have an influence on the bandgap of the compounds. As the layer-number increases, the average Pb/Sn−Br−Pb/Sn angles increase from 171.51° (n=2) to 173.05° (n=3) for the BA alloyed Pb/Sn series and 168.76° (n=2) to 171.40° (n=3) for the 3AMPY series. This suggests that as the inorganic layer grows thicker, the influence of the organic spacer decreases.

Table 3. Comparison of Pb/Sn−Br−Pb/Sn Angles, d-Spacing, bond length distortion, and bond angle variance for $(BA)_2(MA)_{n-1}Pb_xSn_{n-x}Br_{3n+1}$ (n = 1−3) and $(3AMPY)(MA)_{n-1}Pb_xSn_{n-x}Br_{3n+1}$ (n = 1−3), respectively.

Compound	Axial Pb/Sn-Br-Pb/Sn angle (deg)	Equatorial Pb/Sn-Br-Pb/Sn angle (deg)	Average Pb/Sn-Br-Pb/Sn angle (deg)	Adjacent Br-Br Distance (Å)	Stacking Axis (Å)	Bond angle variance (deg^2)	Bond length distortion	Shift factor
$(BA)_2Pb_{0.83}Sn_{0.17}Br_4$ (n=1)		155.8(3)		8.886(6)	20.227(7)	0.3401	0.0041	(0.05,0.05)
$(BA)_2MAPb_{1.31}Sn_{0.69}Br_7$ (n=2)	179.93(10)	163.09(10)	171.51(10)	8.786(4)	31.732(5)	9.7383	0.0131	(0.12,0.12)
$(BA)_2MA_2Pb_{2.02}Sn_{0.98}Br_{10}$ (n=3)	175.25(14)	170.85(10)	173.05(12)	8.833(3)	43.505(4)	12.7891	0.0188	(0.25,0.25)
$(3AMPY)Pb_{0.79}Sn_{0.21}Br_4$ (n=1)		162.42(3)		5.9926(17)	16.106(4)	35.907	0.0115	(0,0.12)
$(3AMPY)MAPb_{1.44}Sn_{0.56}Br_7$ (n=2)	170.02(12)	167.49(7)	168.76	4.252(4)	27.276(4)	11.0041	0.0110	(0,0.15)
$(3AMPY)MA_2Pb_{1.56}Sn_{1.44}Br_{10}$ (n=3)	171.40(4)	171.40(4)	171.40(4)	4.196(12)	39.051(15)	7.881	0.0138	(0,0.25)

The straight chain aliphatic mono-ammonium spacer (BA^+) leads to the expected uniaxial expansion of the layer stacking axis. The interlayer distance (defined as the distance between the planes passing through the terminal bromine atoms of the adjacent $[Pb_xSn_{1-x}Br_6]^{4-}$ layers) between the inorganic lead bromide layers ranges from 8.886 Å (n=1) to 8.786 Å (n=2) and 8.833 Å (n=3) for the BA series. As n increases, the closest Br···Br distance for the BA alloyed lead/tin series (n=1-3) remains almost constant, while it slightly decreases from 5.993 Å for $(3AMPY)Pb_{0.79}Sn_{0.21}Br_4$ (n=1) to 4.252 Å for $(3AMPY)(MA)Pb_{1.44}Sn_{0.56}Br_7$ (n=2) and 4.196 Å for $(3AMPY)MA_2Pb_{1.7}Sn_{1.3}Br_{10}$ (n=3). Moreover, the periodicity along the stacking axis of the studied bilayer lead bromide perovskites ranges from 20.227 Å (n=1) up to 43.505 Å (n=3). It ranges from 16.106 Å (n=1) up to 27.277 Å for (n=2) and 39.051 Å (n=3) for 3AMPY series. Relative to the aliphatic systems, the shorter and doubly charged 3AMPY cation can bring the inorganic layers even closer to one another. To well understand the RP or DJ phase layered hybrid perovskites for these six materials, the value of the shift vector of neighboring layers has been calculated in Table 3. The situation is complicated by the presence of a significant number of structures characterized by “intermediate” values shift vectors different from the "ideal" cases of (1/2, 1/2) for RP and (0, 0) or (0, 1/2)

for DJ phases due to flexibility of organic spacer. Thus, the BA and 3AMPY series exhibit an intermediate RP and DJ phases, respectively.[57]

2.3 Solid-State NMR Analysis of Local Structures and Interactions

By examining the extent of structural distortions, such as variations in bond length and bond angle, across both the in-plane and out-of-plane directions in RP and DJ phases, we have discovered that these structural changes have an impact on the distribution of M-site metal cations in the inorganic layers, as well as on the packing interactions between spacer cations in organic layers and interfaces between them. Understanding the structure of the organic-inorganic interface is particularly important in comprehending the optoelectronic properties and serves as input for electronic structure calculations. However, due to the small scattered intensities associated with light atoms, such as hydrogen, carbon, and nitrogen atoms, the packing arrangements of spacer cations cannot be accurately resolved using conventional single-crystal XRD measurement and analysis. Furthermore, the varying distributions of M-site metal cations could potentially impact the interactions between spacer cations and metal halide octahedra. To investigate these questions, we utilized high-field solid-state NMR spectroscopy, which is well-suited to probing the local chemical bonding environments of organic cations, apical octahedral tilts, and interfaces between them in layered perovskites.[67-70] Specifically, we examined ^{1}H, ^{207}Pb and ^{119}Sn sites and through-space ^{1}H-^{1}H interactions to identify the specific packing interactions.

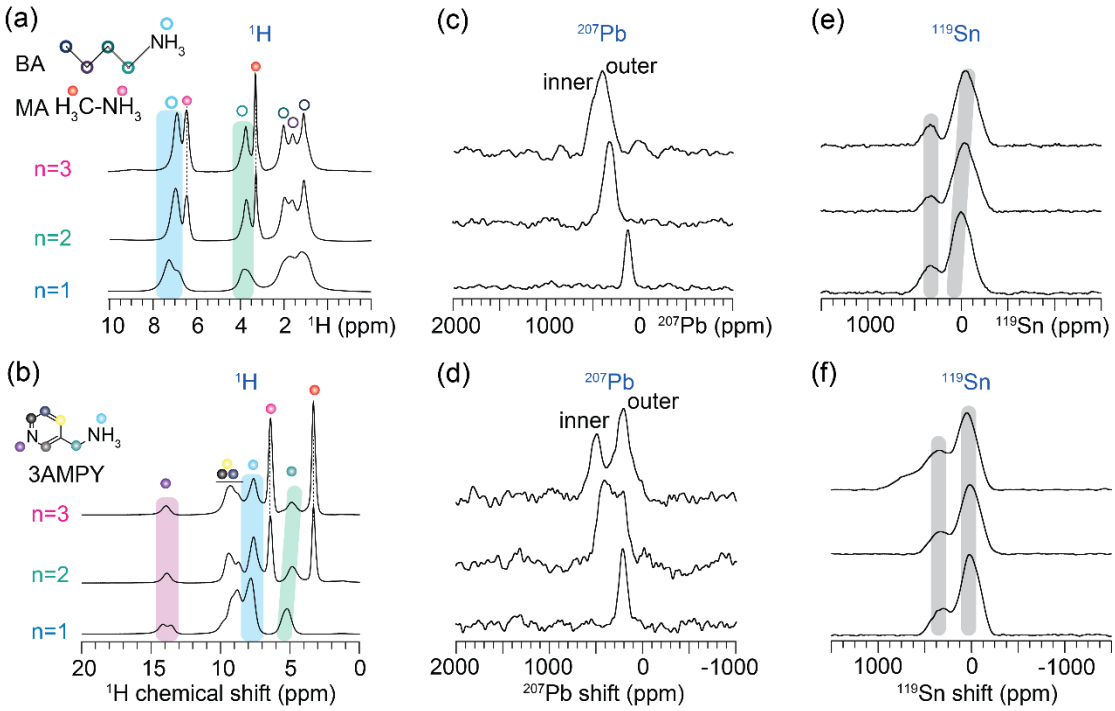

Figure 6. Solid-state 1D (a,b) ^{1}H MAS, (c,d) ^{207}Pb MAS and (e,f) ^{119}Sn MAS NMR spectra of $(BA)_2(MA)_{n-1}Pb_{nx}Sn_{n-nx}Br_{3n+1}$ (n = 1−3) RP phases on top panels, and for $(3AMPY)(MA)_{n-1}Pb_{nx}Sn_{n-nx}Br_{3n+1}$ (n = 1−3) in the lower panels. All spectra were acquired at 18.8 T (^{1}H = 800 MHz) and 50 kHz MAS. The vertical bands indicate the changes in chemical shifts across n=1-3 layered powder compounds.

Figure 6a,b present 1D ^{1}H MAS NMR spectra of $(BA)_2(MA)_{n-1}Pb_xSn_{n-x}Br_{3n+1}$ and $(3AMPY)(MA)_{n-1}Pb_xSn_{n-x}Br_{3n+1}$ (n=1-3), respectively. For n=1, the signals corresponding to different proton sites in BA and 3AMPY cations are observed. For a single NH_3^+ site BA and a single pyridyl NH site in 3AMPY, a pair of signals are observed as indicated by the blue and magenta vertical bands, suggesting different local chemical environments at the organic-inorganic interfaces. For BA spacer cations (n=1), the Δδ (NH_3) of 0.5 (7.3– 6.8) ppm can be attributable to the different noncovalent interactions at the interface. For the pyridyl NH sites of AMPY (n=1), and the chemical shift difference, Δδ(^{1}H) = 14.2 –13.6 = 0.6 ppm, is due to the different hydrogen bonding interactions with the lead/tin bromide octahedra. Although there are expected subtleties in the interactions between NH_3 sites and lead/tin octahedra, these signals are difficult to resolve due to the severe peak overlap in the 7-10 ppm range that originates from NH_3 peaks and pyridyl protons. As a result, the end groups of BA and 3AMPY

cations exhibit distinct experimental signatures related to the proximity of either tin or lead octahedra, which is consistent with the single-crystal analysis presented above. Interestingly, separate spectral signatures are no longer distinctly observed for the n=2, 3 phases (both RP and DJ), and any differences in the $\Delta\delta(NH_3)$ and $\Delta\delta(NH)$ values are expected to be subtle and hidden within the linewidths. However, for the 3AMPY cations, a systematic variation in the CH_2 (turquoise dots) chemical shifts are observed in n=1-3 as shown by a vertical band in the 5-6 ppm (**Figure 6a**), indicating the changes in the local conformations of the Py-CH_2-NH_3 groups. In addition, for the n=2 and 3 samples, narrow signals corresponding to MA^+ cation are observed (red and pink dots), suggesting the isotropic tumbling motions of the A-site cations in the perovskite cages. Thus, the analysis of ^{1}H NMR spectra indicates that the different noncovalent interactions between the spacer cations and metal halide octahedra contribute to the variations in the chemical shifts.[71, 72]

Because of their broad chemical shift range and high sensitivity to changes in the local bonding environments of metal halide octahedra, ^{207}Pb and ^{119}Sn MAS NMR spectra provide information on local structural changes in the inorganic slabs.[67, 73-78] The 1D ^{207}Pb NMR spectra of 3AMPY and BA series are presented in **Figure 6c,d.** For the layered structures of RP phases with different n values, the different distributions of ^{207}Pb shifts are observed in the range of 110-212 ppm, indicating the presence of locally tilted lead octahedra consistently with the single-crystal analyses. In the n=1 layered structures, narrow peaks at 109 ppm (BA) and 212 ppm (3AMPY) indicate highly ordered Pb atoms, and the chemical shift difference of 103 ppm between these two phases is attributed to the different chemical nature of spacer cations and their interactions with the lead octahedra or the different Pb/Sn distributions in a more ordered fashion. For the n=2 layered structures, a relatively broad ^{207}Pb peak centered at 436 ppm is observed for the BA system, while several partially resolved ^{207}Pb signals in the 140-500 range are detected due to the different distributions of axial and equatorial Sn/Pb-Br-Sn/Pb bond angles, which share the interfaces between two different organic cations (MA and BA or 3AMPY cations). Notably, the different chemical distributions of ^{207}Pb and ^{119}Sn atoms in the octahedra contributes to the

displacement of chemical shifts, as will be further confirmed by the changes in the ^{119}Sn chemical shifts discussed below. For the n=3 systems, the 1D ^{207}Pb MAS NMR spectra exhibited further signal broadening or the displacement of chemical shifts and partially resolved line shape indicates two contributions: one is originating from the outer layers exposed to longer spacer cations (~390 ppm), and the other one in the inner layer (~486 ppm) facing towards the MA^+ cations. In the case of $(BA)_2(MA)_{n-1}Pb_{nx}Sn_{n-nx}Br_{3n+1}$ (n=3), the ^{207}Pb signal associated with Pb atoms in the outer layer is observed at a higher frequency than the same atoms in the inner layer, consistently with the literature ^{207}Pb NMR studies of lead iodide-based RP phases.[67, 74] By comparison, the $(3AMPY)(MA)_{n-1}Pb_xSn_{n-x}Br_{3n+1}$(n=3) DJ phase shows two well resolved ^{207}Pb signals corresponding to the inner layer (~486 ppm) and outer layers (~238 ppm), as shown in **Figure 6d** (top). For both BA and 3MAPY (n=3) phases, the ^{207}Pb signals associated with the outer layer are more intense than the inner layers, indicating that the lead atoms are highly populated at the outer layers than the inner layers.

In the 1D ^{119}Sn NMR spectra (**Figure 6e, f**) of the BA and 3AMPY series, peaks characteristic of the octahedral Sn atoms in the (II) oxidation state are observed in the −100 to 400 ppm range.[68, 77, 78] Specifically, the peak at ~0 ppm is due to the Sn atoms in the extended tin bromide network, and the peak at ~350 ppm is hypothesized to originate from the Sn octahedral distributed into the lead octahedra network. For BA systems, the intensity of this latter peak decreases and the peak at ~0 ppm displaces towards lower frequencies (~100 ppm) as the n value increases, suggesting that the inorganic layer thickness influences Pb/Sn distribution in the M-site of the octahedra. By comparison, 3AMPY systems shows a different trend, whereby the intensity of the peak ~350 ppm increases as the n value increases, leading to different distributions of peaks in the 300-800 ppm range. In particular, ^{119}Sn NMR study confirms that more than one type of Sn atoms is present and distributed into the lead octahedra, leading to locally induced structural distortions in the 3AMPY systems, which agrees with the single-crystal XRD diffraction measurements and analyses.

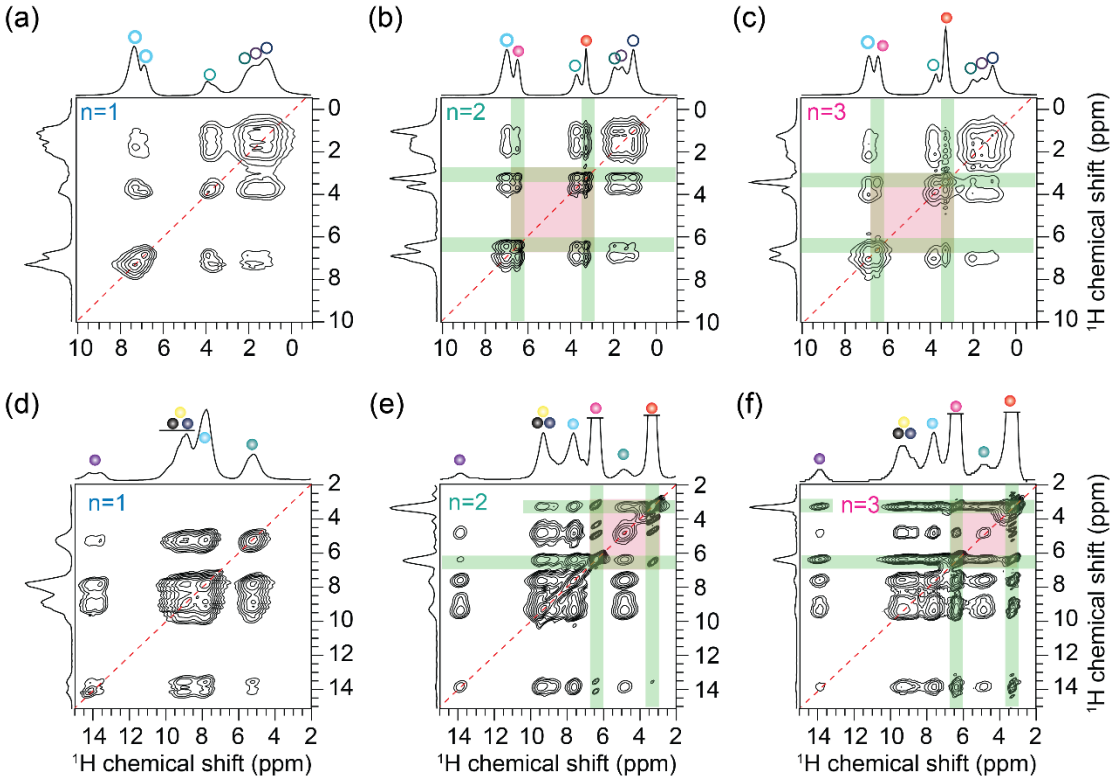

Figure 7. 2D ^{1}H-^{1}H spin diffusion spectrum of $(BA)_2(MA)_{n-1}Pb_{nx}Sn_{n-nx}Br_{3n+1}$ (a) n=1 (b) n=2 (c) n=3 and $(3AMPY)(MA)_{n-1}Pb_{nx}Sn_{n-nx}Br_{3n+1}$ (d) n=1 (e) n=2 and (f) n=3. All spectra were acquired at 18.8 T (^{1}H = 800 MHz) and 50 kHz MAS, and with 500 ms of mixing time. The magenta boxes indicate the peaks correspond to the MA cations, and the horizontal and vertical green bands depict the through space proximity between the large spacer cations and the MA cations.

Further, we carried out 2D ^{1}H-^{1}H spin-diffusion NMR experiments to probe proximities and interactions between the spacer cations and MA^{+} cations in the cuboctahedra voids.[72, 79] In experiments of this type, magnetization exchange takes place between through-space and dipolar coupled spins as a function of spin-diffusion time (also referred to as mixing time), which can propagate from a few angstrom distances to hundreds of nanometers. The resulting 2D spectrum contains on- and off-diagonal peaks, whereby the off-diagonal peaks are characteristic of the magnetization exchange between inter- and intramolecular ^{1}H sites, intensities of which can depend on the mixing time used. For short mixing times (< 20 ms), no off-diagonal peaks are observed, however, longer mixing times of over 100 ms lead to the off-diagonal peaks between the BA-MA and (3AMPY)-MA sites to be detected and resolved. **Figure 7**

shows the 2D ^{1}H-^{1}H spin diffusion NMR spectra acquired with 500 ms mixing time for $(BA)_2(MA)_{n-1}Pb_{nx}Sn_{n-nx}Br_{3n+1}$ and $(3AMPY)(MA)_{n-1}Pb_{nx}Sn_{n-nx}Br_{3n+1}$ (n = 1−3), respectively. For RP and DJ phases (n=1), the nanoscale proximity with the BA^+ spacer cations (i.e., within the organic layer) is established by off-diagonal peaks, and the identical off-diagonal peaks for the $3AMPY^{2+}$ cations are also observed. For the layered RP and DJ phases (n=2, 3), an apparent set of off-diagonal signals (highlighted by the horizontal and vertical green bands) corresponding to the through-space interactions between organic spacer cations (BA^+ or $3AMPY^{2+}$) and MA^+ is observed. Notably, for DJ phases with 3AMPY cations (n=2), relatively weak off-diagonal signals between pyridyl NH sites of spacer cations and MA^+ protons are due to the poor spacer cation ordering at the organic-inorganic interface. The magenta boxes indicate the MA-MA proximities within the perovskite layer.

2.4 Optical Properties and Work Functions

As discussed above, the $(BA)_2(MA)_{n-1}Pb_xSn_{n-x}Br_{3n+1}$ series powder compounds has larger octahedral tilts, resulting in larger bandgaps than the $(3AMPY)(MA)_{n-1}Pb_xSn_{n-x}Br_{3n+1}$ series.[80, 81] The absorption spectra of both RP and DJ series powder compounds show a high-energy absorption edge and a lower energy exciton peak (**Figure 8a,c**). The exciton absorption bandgaps are estimated by extrapolating the high-energy slope to the imaginary axis parallel to the x axis where the absorption edge is interrupted by the exciton peak.[30, 54] The bandgaps of the $(BA)_2(MA)_{n-1}Pb_xSn_{n-x}Br_{3n+1}$ series decrease from 2.47 eV to 1.97 eV for n = 1−3, while those for the $(3AMPY)(MA)_{n-1}Pb_xSn_{n-x}Br_{3n+1}$ series decline from 2.41 eV to 1.86 eV for n = 1−3. In addition to the differences in bandgap, there is also a change in the exciton binding energy as shown in **Table 4**.

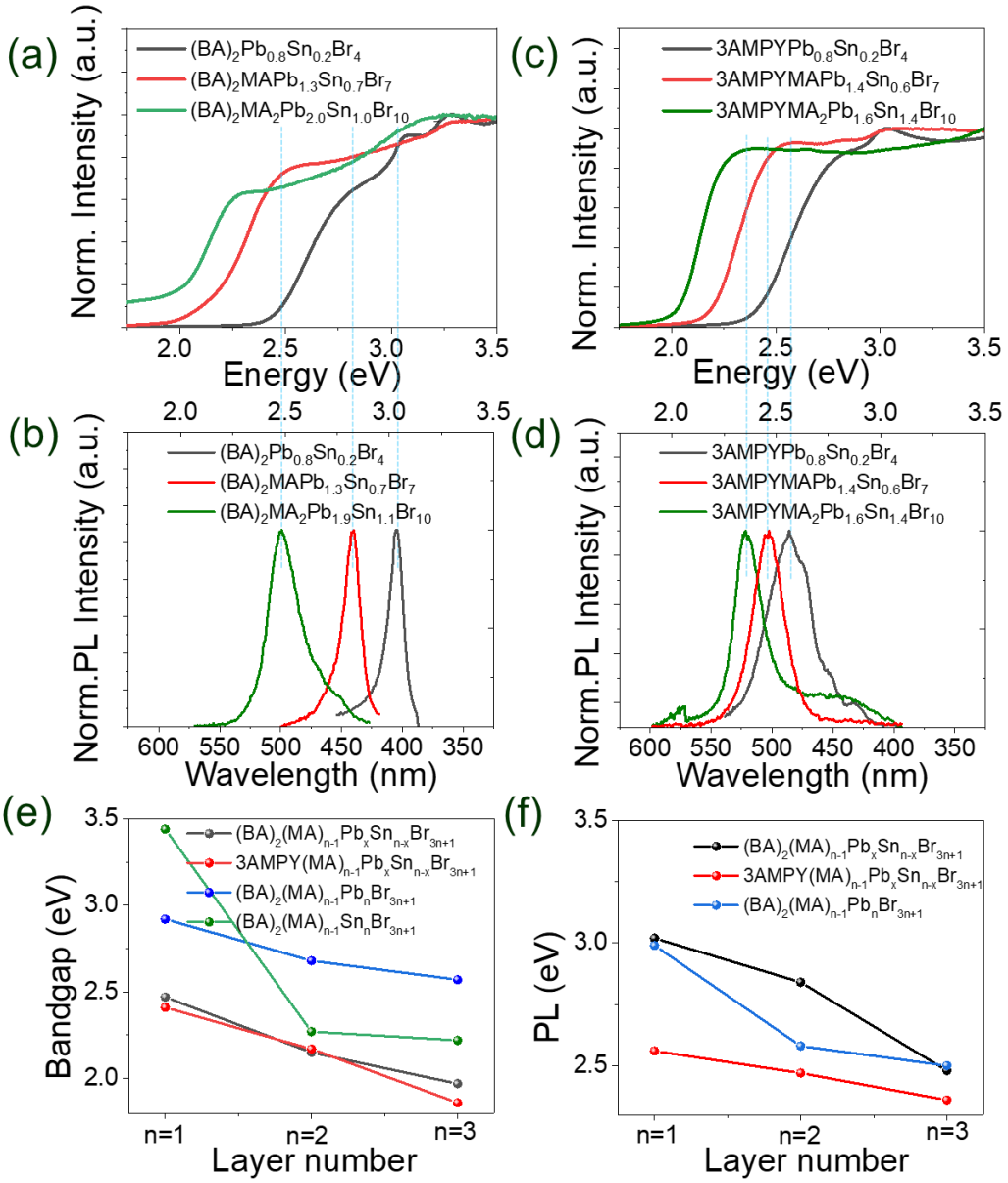

Figure 8. Optical absorption and steady-state photoluminescence (PL) spectra for (a, b) $(BA)_2(MA)_{n-1}Pb_xSn_{n-x}Br_{3n+1}$, (c, d) $3AMPY(MA)_{n-1}Pb_xSn_{n-x}Br_{3n+1}$ (n = 1−3) series and (e, f) optical bandgap values extrapolated from the edge of the absorption spectra and positions of the maxima of the PL spectra for the corresponding $(BA)_2(MA)_{n-1}Pb_xSn_{n-x}Br_{3n+1}$ series, pure tin $(BA)_2(MA)_{n-1}Sn_nBr_{3n+1}$ powder compounds and pure lead $(BA)_2(MA)_{n-1}Pb_nBr_{3n+1}$ powder compounds, respectively.

Table 4. Optical band-gaps, energy at maximum PL, full width at half maximum of PL, and average effective mass of the compounds calculated based on the for $(BA)_2(MA)_{n-1}Pb_xSn_{n-x}Br_{3n+1}$ (n = 1−3) and $(3AMPY)(MA)_{n-1}Pb_xSn_{n-x}Br_{3n+1}$ (n = 1−3) powder compounds, respectively.

Compound	Band gap E_g (eV)	Excitonic absorption (eV)	PL(eV)	FWHW eV (nm)	Color
$(BA)_2Pb_{0.8}Sn_{0.2}Br_4$ (n=1)	2.47	3.19	3.02	0.08(10.81)	yellow
$(BA)_2MAPb_{1.3}Sn_{0.7}Br_7$ (n=2)	2.15	3.02	2.84	0.11(37.52)	Light orange
$(BA)_2MA_2Pb_{1.9}Sn_{1.1}Br_{10}$ (n=3)	1.97	2.77	2.48	0.19(37.52)	Dark Orange
$(3AMPY)Pb_{0.8}Sn_{0.2}Br_4$ (n=1)	2.41	2.94	2.56	0.23(43.43)	Light orange
$(3AMPY)MAPb_{1.5}Sn_{0.5}Br_7$ (n=2)	2.17	2.78	2.47	0.18(36.63)	Light red
$(3AMPY)MA_2Pb_{1.7}Sn_{1.3}Br_{10}$ (n=3)	1.86	2.95	2.36	0.16(35.36)	Red
$(BA)_2PbBr_4$ (n=1)	2.92	3.19 (SI)	2.92[82]	0.22(29.56)	White
$(BA)_2MAPb_2Br_7$[35] (n=2)	2.68	2.81	2.58[61]	0.26(57.09)	Yellow
$(BA)_2MA_2Pb_3Br_{10}$ (n=3)	2.57	2.94	2.50	0.09(15.70)	Orange
$(BA)_2SnBr_4$ (n=1)	3.44		2.36		
$(BA)_2MASn_2Br_7$ (n=2)	2.27		2.82		Yellow
$(BA)_2MA_2Sn_3Br_{10}$ (n=3)	2.22		2.71		Orange

The organic spacer influences the luminescent properties of the materials mainly through their modes of interaction with the inorganic framework and the resulting distortions in the perovskite M−Br−M bridging angles.[83] As seen in **Figure 8b,d**, the 2D bilayer perovskites display strong PL emission with an emission energy close to the energy value of the excitonic peak in the absorption spectra.[54] The maximum of PL emission peak of $(BA)_2(MA)_{n-1}Pb_xSn_{n-x}Br_{3n+1}$ series is centered at 3.02 eV (n=1, x=0.83), 2.84 eV (n=2, x=1.31) and 2.48 eV (n=3, x=2.02). In the $(3AMPY)(MA)_{n-1}Pb_xSn_{n-x}Br_{3n+1}$ series, the maximum of PL emission peak is centered at 2.56 eV (n=1, x=0.79), 2.47 eV (n=2, x=1.71) and 2.36 eV (n=3, x=1.56), and all of

which are lower energies than that of $(BA)_2(MA)_{n-1}Pb_xSn_{n-x}Br_{3n+1}$ series. The PL peak positions of the $(BA)_2(MA)_{n-1}Pb_xSn_{n-x}Br_{3n+1}$ series and $(3AMPY)(MA)_{n-1}Pb_xSn_{n-x}Br_{3n+1}$ series locate between the exciton absorption peak and bandgap. The Full Width Half Maximum (FWHM) of PL emission increases from 0.08 eV (10.81 nm, n=1) to 0.19 eV (37.52 nm, n=3) for $(BA)_2(MA)_{n-1}Pb_xSn_{n-x}Br_{3n+1}$ series with the increased layer numbers due to the increased bond angle variance. On the contrary, the FWHM of PL emission decreases from 0.23 eV (43.43 nm, n=1) to 0.16 eV (35.36 nm, n=3) for $(3AMPY)(MA)_{n-1}Pb_xSn_{n-x}Br_{3n+1}$ series with the increased layer numbers due to the reduced bond angle variance.

It is noteworthy to drawing comparison between the pure lead bromide and pure tin bromide analogues. From the previous report results, the BA cations can form 2D $(BA)_2PbBr_4$, but it can be both stabilized with 0D $(BA)_2SnBr_6$ and 2D $(BA)_2SnBr_4$. The photo-physical characterization of the other 2D pure lead $(BA)_2(MA)_{n-1}Pb_nBr_{3n+1}$ series (n=2, 3) are shown in **Figure 8e,f**. The absorption bandgap and exciton absorption peak are located at 2.68 eV and 2.81 eV for pure lead $(BA)_2(MA)_{n-1}Pb_nBr_{3n+1}$ (n=2), 2.57 eV and 2.94 eV for pure lead $(BA)_2(MA)_{n-1}Pb_nBr_{3n+1}$ (n=3), respectively. The bandgaps for 2D alloyed Pb/Sn series are broader than those of pure lead $(BA)_2(MA)_{n-1}Pb_nBr_{3n+1}$ series (**Figure S3**), consistent with the 3D mixed Sn and Pb perovskites.[84] In order to investigate the dependence of optical properties on the different ratio Pb/Sn composition based on the BA cations (n=3). We exploit the fact that, the energy band gaps of the mixed Pb/Sn compounds do not follow a linear trend (the Vegard's law) in between these two extremes of 2.07 ($(BA)_2MA_2Sn_3Br_{10}$), and 2.50 eV ($(BA)_2MA_2Pb_3Br_{10}$), respectively, but have narrower bandgap of 1.89 eV when we enriched Sn in Pb compounds (Sn:Pb = 0.8:0.2), which is consistent with the related report.[41]

As a comparison, the PL peak positions of the 2D pure lead series (n=2) exhibit higher energy compared to their corresponding bandgap,[35] which is a bit different from the BA alloyed Pb/Sn compounds. The photoluminescence lifetime is an important property of the emission process and of broad interest in the perovskite community especially for probing the excited state dynamics and for device applications. To our

knowledge, there is no systematic study of how photoexcited carriers behave in multilayer 2D alloyed Pb/Sn bromide crystals. Time-resolved PL measurements were conducted to understand better how long excitons last in these 2D materials (see the Supplementary Information for details). The PL lifetimes of the (3AMPY)$(MA)_{n-1}Pb_xSn_{n-x}Br_{3n+1}$ series (10-20 ns) are much longer than those in the $(BA)_2(MA)_{n-1}Pb_xSn_{n-x}Br_{3n+1}$ series (2-5 ns) (**Table 5** and **Figure S4**). This suggests slower carrier recombination and improved carrier transport. This improvement could be due to the presence of the aromatic cation in 3AMPY, thanks to the delocalized π-electron cloud, which created a barrier with a larger dielectric constant (εb ~ 3) than the aliphatic BA barrier (εb ~ 2). As a result, the dielectric mismatch between organic and inorganic sections is reduced, and the corresponding dielectric confinement effect is less pronounced in the DJ structures. The PL lifetime becomes larger from 2.78 ns to 4.77 ns for RP cases and 10.25 ns to 18.80 ns for DJ cases as the thickness (n) of the layers increases due to the formation of less confined quantum-well structures. [85, 86]

Considering these newly synthesized perovskite compounds could be used in future devices, thus it is important to know the energy positions of their valence/conduction bands to design optimal interfaces and device assembly. The valence band maximum (VBM) of the different compounds is measured by photoemission yield spectroscopy in air (PYS) (**Figure S5**). The conduction band minimum (CBM) is calculated from the difference between the VBM and the band-gap. We also compare the VBM and CBM of the three compounds with $PbBr_2$, 3D $MAPbBr_3$, $CsPbBr_3$ and pure lead $(BA)_2(MA)_{n-1}Pb_nBr_{3n+1}$ series compounds (n=1-3).[87] The alloyed $(BA)_2(MA)_{n-1}Pb_xSn_{n-x}Br_{3n+1}$ series (n=1-3) have a strong energy variation in the VBM (5.90 eV for BA Pb Sn n=1, 5.72 eV for BA Pb Sn n=2, and 5.55 eV for BA Pb Sn n=3), whereas the CBMs for $(BA)_2(MA)_{n-1}Pb_xSn_{n-x}Br_{3n+1}$ series (n=2-3) remain almost constant. The (3AMPY)$(MA)_{n-1}Pb_xSn_{n-x}Br_{3n+1}$ series (n=1-3) also have an energy variation in the VBM (5.85 eV for (3AMPY) Pb/Sn n=1, 5.69 eV for (3AMPY) Pb/Sn n=2, and 5.60 eV for (3AMPY) Pb/Sn n=3) and CBM (3.48 eV for (3AMPY) Pb/Sn n=1, 3.50 eV for (3AMPY) Pb/Sn n=2, and 3.59 eV for (3AMPY) Pb/Sn n=3). Compared with $PbBr_2$, 3D $CsPbBr_3$ and $MAPbBr_3$, the CBMs for these compounds are similar to 3D $MAPbBr_3$,

while the VBM for the three compounds are larger than those of $PbBr_2$ and 3D $CsPbBr_3$ and $MAPbBr_3$. Compared to the pure lead $(BA)_2(MA)_{n-1}Pb_nBr_{3n+1}$ series compound (n=1-3), the CBMs of which (2.94 eV for BA Pb n=1, 3.00 eV for BA Pb n=2, and 3.15 eV for BA Pb n=3) are smaller than the corresponding alloyed Pb/Sn compounds based on BA cations, and the CBMs (5.87 eV for BA Pb n=1, 5.68 eV for BA Pb n=2, and 5.59 eV for BA Pb n=3) are comparable to those of $(BA)_2(MA)_{n-1}Pb_xSn_{n-x}Br_{3n+1}$ series (n=1-3). It is evident that the 2D alloyed Pb/Sn compounds show a narrower bandgap than the pure lead $(BA)_2(MA)_{n-1}Pb_nBr_{3n+1}$ series compounds. Thus, the different cations and A-site metal cation show a significant influence on the VBM and CBM, which is an important factor for the correct interface assembly. We also investigated the stability of the alloyed Pb/Sn bromide perovskite compounds in the air (temperature, 22 °C; humidity, 45-60%) for one month. All the XRD results show that the compounds remain almost constant for one month except the $(BA)_2(MA)Pb_xSn_{n-x}Br_7$ sample which exhibited some extra peaks of $(BA)_2Pb_xSn_{n-x}Br_4$ (**Figure S6**). Thus, the alloyed Pb/Sn bromide perovskite compounds exhibit excellent structural stability.

2.5 Electronic Band Structure Calculations

We use density functional theory calculations (DFT, see experimental section) to explore the thermodynamic stability of n=1 alloys $APb_{1-x}Sn_xBr_4$ (A=BA or 3AMPY) depending on the Pb/Sn ratio. Calculations are performed on a series of model systems with cesium ions emulating the organic cations in order to describe the formation of the mixed-metal perovskite starting from well-defined salts, which have not been reported for $(BA)_2Br$ or (3AMPY)Br (**Figure S7**). For each Pb/Sn ratio, we consider several distributions of Pb and Sn metal cations and report only the lowest energy optimized structure. Then, the Gibbs free energy of formation starting from reference salts $PbBr_2$, $SnBr_2$ and CsBr is computed using the following approximate expression:

$$\Delta G(x) = E(Cs_2Pb_{1-x}Sn_xBr_4) - 2E(CsBr) - (1-x)E(PbBr_2) - xE(SnBr_2) - TS_{mix}(x),$$

Where $E(Cs_2Pb_{1-x}Sn_xBr_4)$ is the total energy per formula unit of the mixed-metal compound, $E(CsBr)$, $E(PbBr_2)$ and $E(SnBr_2)$ the ones of the salts and $S_{mix}(x)$ the mixing entropy given, in the mean-field approximation, by:

$$S_{mix}(x) = -k_B[x \ln x + (1-x)\ln(1-x)],$$

with k_B the Boltzmann constant. Such a form for the Gibbs free energy is obtained when regarding CsBr, $PbBr_2$ and $SnBr_2$ as infinite reservoirs and prevent us from exploring specific synthetic conditions that could be Pb-rich or Sn-rich.

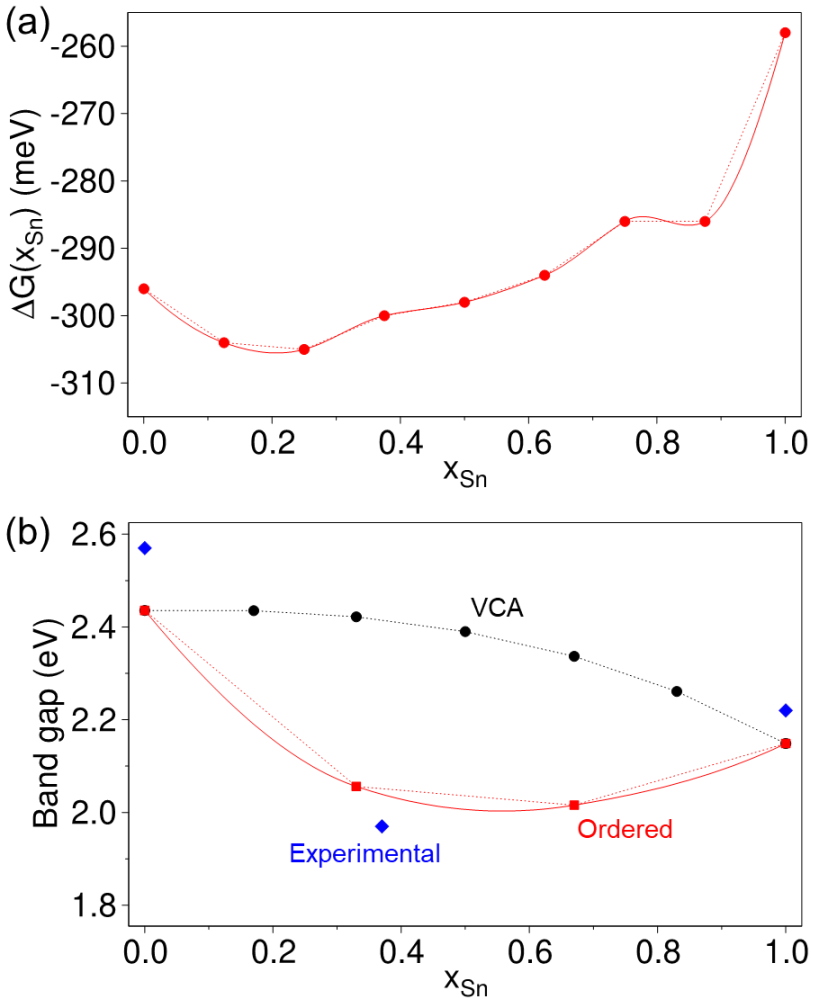

Figure 9. (a) Computed Gibbs free energy of n=1 model systems $Cs_2Pb_{1-x}Sn_xBr_4$ at room temperature. For each value of x, various distributions of Pb and Sn are obtained, only the lowest energies are reported. The plain red line is obtained by interpolation. A global minimum is found around x=0.2 , and a shallow one around x=0.9, indicating a thermodynamic advantage for Pb-rich (and Sn-rich) compounds over the 50:50 alloys. (b) Experimental band gaps of n=3 series $(BA)_2(MA)_2Pb_{3(1-x)}Sn_{3x}Br_{10}$ (blue diamonds). Band gaps of model n=3 systems $Cs_4Pb_{3(1-x)}Sn_{3x}Br_{10}$ calculated using the virtual crystal approximation (VCA, black circles) and supercells containing twelve metallic sites (red squares). Only the lowest energy structures are

reported. A rigid shift of 1.2 eV has been applied to the calculated band gaps. The VCA description shows a continuous decrease of the bandgap going from pure Pb to pure Sn structures, whereas the ordered structures exhibit the band bowing experimentally observed and described in 3D mixed-metal halide perovskites.

The computed Gibbs free energy shows a trend toward Pb-rich alloys with a minimum around x=0.2, which fits well with the experimentally obtained n=1 compounds. Interestingly, by considering the stability of the mixed-metal perovskite over pure-lead and pure-tin structures (**Figure S8**), we recover similar trends with a global minimum for the Pb-rich composition over the 50:50 alloy. Naturally, the nature of the model, and in particular, the use of cesium cations substituting organic cations could modify the energetic landscape. In that regard, we note that similar Pb/Sn ratio are found for n=1 compounds, independently of the organic cation used. Thus, the presence of Pb-rich layered perovskite seems to be thermodynamically driven. A very shallow local minimum is also present for Sn-rich compounds, which might be obtained. However, 50/50 alloys appear thermodynamically unfavored for n=1 compounds.

DFT calculations on model systems also shed light on the experimentally observed evolution of the band gap with Pb:Sn ratio. In the case of n=3 structures, we use two different approaches to describe mixed Pb/Sn systems in the model system $Cs_4Pb_{3(1-x)}Sn_{3x}Br_{10}$. Firstly, we use the virtual crystal approximation (VCA), where we place a virtual atom with mixed Pb and Sn character at the metal site. This approach is used to describe solid solution in which there is no ordering of Sn and Pb ions. In a second approach, we use a supercell of the model n=3 system counting 12 metallic sites and experience various distributions of Pb and Sn ions for a given value of x, allowing us to assess the effect of ordering on the electronic structure. **Figure 9b** presents both sets of computed results compared with the experimental band gaps extracted from **Figure 8e** for the complete n=3 BA series. While, the VCA description shows a continuous decrease of the bandgap going from pure Pb to pure Sn structures, the ordered structure approach displays mixed-metal structures with a lower band gap than the pure-metal compounds. This electronic band bowing is consistent with the experimental observation on the optical band gaps for n=3 compounds and has been previously

described in 3D mixed-metal Pb/Sn halide perovskites.[46, 88] In the 3D compounds, the effect seems to originate from local distortions caused by for short-range orderings. In our rough preliminary model, the closing of the band gap can be traced back to a dealignment of Pb and Sn states, an extreme example of which is depicted **Figure S9** for the x=0.33 model system. In this case, the Pb (Sn) electronic substructure, i.e. electronic states dominated by Pb (Sn) contributions, shows a bandgap of 1.63 eV (1.45 eV), but, because of the relative shift of Pb and Sn states this leads to a global band gap of only 0.86 eV. This promising preliminary investigation appeals for a more complete investigation of the electronic structure of layered mixed-metal halide perovskites.

2.6 Crystal Orientation in the Thin-Film Examined by GIWAXS.

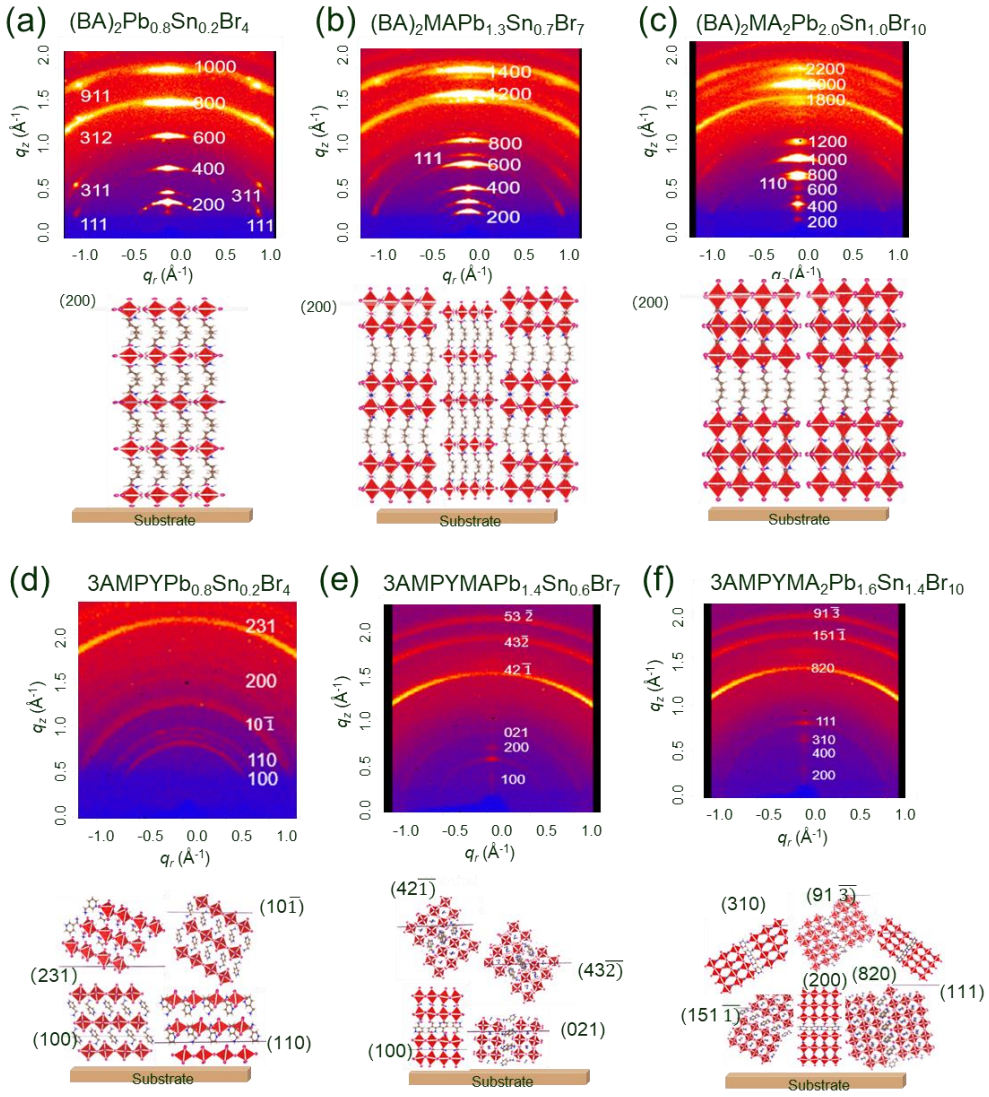

Figure 10. Synchrotron GIWAXS patterns and different thin-film growth orientations

of (a-c) $(BA)_2(MA)_{n-1}Pb_xSn_{n-x}Br_{3n+1}$ and (d-f) $(3AMPY)(MA)_{n-1}Pb_xSn_{n-x}Br_{3n+1}$ (n = 1-3) series compounds, respectively. The (h00) planes show in-plane orientation- and (0hh) planes have out-of-plane orientation with peaks labeled.

To create high-performance optoelectronics devices that make full use of carriers traveling through inorganic layers, it is crucial to comprehend and manage the crystal orientation in films, given the two-dimensional nature of the compounds. Solar cells, light-emitting diodes, and photodetectors require charge currents that move perpendicular to the film to operate, whereas thin-film transistor devices require in-plane transport. Hence, we utilized GIWAXS analysis to evaluate the crystallinity and orientation of the thin films. GIWAXS patterns for the $(BA)_2(MA)_{n-1}Pb_nBr_{3n+1}$ and $(3AMPY)(MA)_{n-1}Pb_nBr_{3n+1}$ films (n=1-3) show Debye-Scherrer diffraction rings with some discrete Bragg spots (**Figure 10**). The GIWAXS data are consistent with the conventional PXRD results (**Figure S10**) obtained from the same thin-films, where the $(BA)_2(MA)_{n-1}Pb_nBr_{3n+1}$ film shows (200), (400), and (600) peaks (for the labeling of the diffraction planes). The (*h*00) peaks correspond to the spots below q_z=2 in GIWAXS patterns. The occurrence of all the peaks along the q_z direction indicates that the $(BA)_2(MA)_{n-1}Pb_nBr_{3n+1}$ film has highly aligned orientations parallel to the substrate. On the contrary, the GIWAXS images for $(3AMPY)(MA)_{n-1}Pb_nBr_{3n+1}$ films show diffraction rings with some stronger intensities along certain extended arc segments, which suggests the thin-films are polycrystalline with almost random orientations. This enables charge carriers to transport along both parallel and perpendicular directions by providing multiple pathways. The GIWAXS data are consistent with the conventional PXRD results (Figure 8d) obtained from the same thin-films, where the $(3AMPY)(MA)_{n-1}Pb_nBr_{3n+1}$ (n=1) film shows (100), (110), and (231) peaks, the $(3AMPY)(MA)_{n-1}Pb_nBr_{3n+1}$ (n=2,3) film shows some (021) and (432) peaks. Future studies will focus on understanding how solvents affect crystalline orientation in these films.

3. Conclusions

Hybrid, thick-layer alloyed Pb/Sn bromide perovskites are an appealing family of 2D perovskites that offer a versatile platform to engineer the structure-property relationships through compositional tuning of the organic spacer cation, the metal cation and the inorganic layer thickness. The new members of the mixed Pb/Sn 2D RP $(BA)_2(MA)_{n-1}Pb_xSn_{n-x}Br_{3n+1}$ and DJ phases $(3AMPY)(MA)_{n-1}Pb_xSn_{n-x}Br_{3n+1}$ presented here offer insight into their chemical nature, packing interactions, structural features, and optoelectronic properties. The studied 2D RP and DJ alloyed Pb/Sn bromide perovskites exhibit desirable low bandgap (1.86 eV -2.47 eV) for light-emission. The aliphatic monoammonium BA cations and the aromatic diammonium 3AMPY cations are incorporated into the mixed Pb/Sn halide perovskite network. As the layer thickness (n) increases, the distortions of the $[Pb_xSn_{1-x}Br_6]^{4-}$ octahedra in both series perovskites increase. The bandgap energies of the Pb/Sn bromide perovskites range from 2.00 to 2.50 eV and exhibit narrow-band emission due to the presence of excitons at room temperature. The carrier lifetimes of the DJ phases $(3AMPY)(MA)_{n-1}Pb_xSn_{n-x}Br_{3n+1}$ (10-20 ns) are longer than those (2-5 ns) of $(BA)_2(MA)_{n-1}Pb_xSn_{n-x}Br_{3n+1}$ RP phases. Our study also shows that Pb-rich alloys (Pb:Sn ~4) for n=1 compounds are thermodynamically favored over 50:50 (Pb:Sn ~1) structures. For both BA and 3MAPY (n=3) systems, the ^{207}Pb NMR signals associated with the outer layer are more intense than the inner layers, indicating that the Pb atoms are highly populated at the outer parts of the layers. Moreover, the solution processability of these materials enables the deposition of thin films, where the GIWASX analysis indicates that the film orientation behavior of the RP and DJ phases exhibit noticeable divergence, which can serve as a valuable reference for developing optoelectronic devices. Overall, this work provides a systematic understanding of the effects of alloying the metal cation in bulk and thin film 2D RP and DJ mixed Pb/Sn halide perovskites, which could serve as highly desirable, low bandgap materials for optoelectronic applications.

4. Experimental Section

Synthesis

Synthesis of $(BA)_2(MA)_{n-1}Pb_xSn_{n-x}Br_{3n+1}$ and $(3AMPY)(MA)_{n-1}Pb_xSn_{n-x}Br_{3n+1}$ (n = 1−3) series.

General Procedure for n=1 $(BA)_2Pb_{0.83}Sn_{0.17}Br_4$ and $(3AMPY)Pb_{0.79}Sn_{0.21}Br_4$: 1116 mg (5 mmol) of PbO, and 1128.25 mg (5 mmol) of $SnCl_2{\cdot}2H_2O$ were dissolved in 25 mL

of hydrobromic acid (HBr) by heating to boiling under constant magnetic stirring, until a clear, transparent solution was obtained. Next, in a separate vial, 985 µL (9.85 mmol) of butylamine ($C_4H_9NH_2$) were added to 50% aqueous H_3PO_2 (2.5 mL). 224 mg (0.5 mmol) of PbO, and 225 mg (0.5 mmol) of $SnCl_2{\bullet}2H_2O$ were dissolved in 5 mL of hydrobromic acid (HBr) by heating to boiling under constant magnetic stirring, until a clear, transparent solution was obtained. Next, in a separate vial, 50 µL (0.5 mmol) of 3-(amino methyl)pyridinium (3AMPY) was added to 50% aqueous H_3PO_2 (1 mL).

General Procedure for n = 2 $(BA)_2(MA)Pb_{1.31}Sn_{0.69}Br_7$ and (3AMPY)MA $Pb_{1.44}Sn_{0.56}Br_7$: 1116 mg (5 mmol) of PbO, 1128.25 mg (5 mmol) of $SnCl_2{\cdot}2H_2O$, and 337.5 mg (2.5 mmol) of MACl powders were dissolved in 25 mL of hydrobromic acid (HBr) by heating to boiling under constant magnetic stirring, until a clear, transparent solution was obtained. Next, in a separate vial, 738 µL (7.38 mmol) of butylamine ($C_4H_9NH_2$) were added to 50% aqueous H_3PO_2 (2.5 mL). 224 mg (0.5 mmol) of PbO, 225 mg (0.5 mmol) of $SnCl_2{\cdot}2H_2O$, and 67.5 mg (0.5 mmol) of MACl powders were dissolved in 5 mL of hydrobromic acid (HBr) by heating to boiling under constant magnetic stirring, until a clear, transparent solution was obtained in the sand bath. Next, in a separate vial, 55 µL (0.51 mmol) of 3-(amino methyl)pyridinium (3AMPY) was added to 50% aqueous H_3PO_2 (1 mL).

General procedure for n=3 $(BA)_2(MA)_2Pb_{2.02}Sn_{0.98}Br_{10}$ and (3AMPY)$(MA)_2Pb_{1.56}Sn_{1.44}Br_{10}$: 1116 mg (5 mmol) of PbO, 1128.25 mg (5 mmol) of $SnCl_2{\cdot}2H2O$, and 337.5 mg (2.5 mmol) of MACl powders were dissolved in 25 mL of hydrobromic acid (HBr) by heating to boiling under constant magnetic stirring, until a clear, transparent solution was obtained. Next, in a separate vial, 450 µL (4.5 mmol) of butylamine ($C_4H_9NH_2$) were added to 50% aqueous H_3PO_2 (2.5 mL). 224 mg (0.5 mmol) of PbO, 225 mg (0.5 mmol) of $SnCl_2{\cdot}2H_2O$, and 67.5 mg (0.5 mmol) of MACl powders were dissolved in 3 mL of hydrobromic acid (HBr) by heating to boiling under constant magnetic stirring, until a clear, transparent solution was obtained in the sand bath. Next, in a separate vial, 20 µL (0.3 mmol) of 3-(amino methyl)pyridinium (3AMPY) was added to 50% aqueous H_3PO_2 (1 mL).

After 10−15 min, stirring was stopped for all the above solutions, the temperature was reduced to 120 °C (as indicated on hot plate), below the boiling point of HBr and kept constant for several days until the first light-yellow crystals seeds started to grow. The temperature was decreased to 95 °C (as indicated on hot plate) and kept constant

for several days to induce stronger precipitation and faster crystal growth. Following this, the hot plate was turned off and the reaction solution was left to cool to room temperature for the completion of the precipitation and crystal growth. The crystals were isolated by vacuum filtration and dried under vacuum overnight.

Single-Crystal X-ray Crystallography:

Single-crystal XRD experiments were performed using a STOE IPDS II or IPDS 2T diffractometer with Ag Kα radiation (λ = 0.5608 Å) operating at 50 kV and 40 mA. Integration and numerical absorption corrections were performed using X-AREA, X-RED, and XSHAPE programs. The structures were solved by charge flipping and refined using the full-matrix least-squares in Olex2. The PLATON software was used to identify the twinning domains and validate the space groups of the compounds. GIWAXS measurements: The film samples were exposed to under the same instrument with LaB6 beam source.

Solid-state NMR spectroscopy*:*

For ssNMR analysis, polycrystalline DJ and RP materials with different n values were prepared in an identical manner for XRD measurements. Samples were separately packed into zirconia rotors of outer diameter 1.3 mm fitted with VESPEL® caps. All solid-state MAS NMR experiments were carried out using 18.8 T (^{1}H = 800.1 MHz, ^{119}Sn = 298.4 MHz and ^{207}Pb = 167.5 MHz) Bruker Avance Neo NMR spectrometer equipped with a 1.3-mm H-X probehead. Unless otherwise specified, all the samples were spun at a MAS frequency of 50 kHz. 1D ^{1}H MAS NMR spectra were acquired by co-adding 16 transients. The relaxation delays were set to 7 s for $(BA)_2(MA)_{n-1}Pb_{nx}Sn_{n-nx}Br_{3n+1}$ and 20 s for $(3AMPY)(MA)_{n-1}Pb_{nx}Sn_{n-nx}Br_{3n+1}$ (n=1-3), as determined from saturation recovery measurements and analyses. The 1D ^{207}Pb and ^{119}Sn MAS NMR experiments were carried out using a spin-echo pulse sequence. 1D ^{207}Pb MAS spectra were with 5120 co-added transients using a relaxation delay of 500 ms and 1D ^{119}Sn MAS NMR spectra were acquired by co-addition of 2048 transients using a relaxation delay of 500 ms. 2D ^{1}H-^{1}H spin diffusion NMR experiments were acquired using a three-pulse noesy-like sequence with 500 ms of mixing times. A rotor-synchronized increment of 20 μs was applied to detect 100 t_1 increments, each with 2 co-added transients. The experimental ^{1}H chemical shifts were calibrated with respect to that of

neat TMS using adamantane as an external reference (^{1}H resonance, 1.82 ppm). The experimental ^{207}Pb and ^{119}Sn shifts were calibrated using $Pb(NO_3)_2$ and $Sn(CH_3)_4$ as external standards according to IUPAC recommendations. [89]

Film Fabrication. FTO glass substrates were first cleaned by sequential sonication in acetone and isopropanol for 15 min each. Subsequently, the FTO substrates were dried with nitrogen and treated for 30 min using ultraviolet ozone (UVO). Solutions of the studied materials were prepared by dissolving 100 mg of dried crystals in 1 mL of anhydrous DMF solvent. The substrates were heated at 130 °C on a hot plate for 10 min under N_2 atmosphere. Then, the precursor solution was spin-coated at 5000 rpm for 30 s in a glovebox under a N_2 atmosphere.

Accession Codes

CCDC 2256571-2256576 contain the supplementary crystallographic data for this paper.

AUTHOR INFORMATION

Corresponding Authors

Mercouri G. Kanatzidis − Department of Chemistry, Northwestern University, Evanston, Illinois 60208, United States; orcid.org/0000-0003-2037-4168; Email: mkanatzidis@northwestern.edu ORCID: 0000-0003-2037-4168

Authors

Ping Fu- *State Key Laboratory of Catalysis, Dalian Institute of Chemical Physics, Chinese concluAcademy of Sciences, Dalian National Laboratory for Clean Energy, 457 Zhongshan Road, Dalian 116023, China* ORCID: 0000-0002-7454-5754

Michael A. Quintero- *Department of Chemistry, Northwestern University, Evanston, Illinois 60208, USA.* ORCID*: 0000-0002-0709-1676*

Eugenia Vasileiadou- *Department of Chemistry, Northwestern University, Evanston, Illinois 60208, USA.* ORCID: 0000-0002-5714-9207

Parth Raval- *University of Lille, CNRS, Centrale Lille, Univ. Artois, UMR 8181 – UCCS – Unité de Catalyse et Chimie du Solide, F-59000 Lille, France.* ORCID: 0000-

0003-2991-4490

Claire Welton- *University of Lille, CNRS, Centrale Lille, Univ. Artois, UMR 8181 – UCCS – Unité de Catalyse et Chimie du Solide, F-59000 Lille, France.* ORCID:

Mikaël Kepenekian- *Univ Rennes, ENSCR, INSA Rennes, CNRS, ISCR (Institute des Sciences Chimiques de Rennes), UMR 6226, France.* ORCID: 0000-0001-5192-5896

George Volonakis- *Univ Rennes, ENSCR, INSA Rennes, CNRS, ISCR (Institute des Sciences Chimiques de Rennes), UMR 6226, France.* ORCID: 0000-0003-3047-2298

Jacky Even- *Univ Rennes, INSA Rennes, CNRS, Institute FOTON - UMR 6082, Rennes, France.* ORCID: 0000-0002-4607-3390

Yukun Liu- *Department of Electrical and Computer Engineering, Northwestern University, Evanston, Illinois 60208, United States* ORCID:

Christos Malliakas-*Department of Chemistry, Northwestern University, Evanston, Illinois 60208, USA.* ORCID: 0000-0003-4416-638X

Yi Yang-*Department of Chemistry, Northwestern University, Evanston, Illinois 60208, USA.* ORCID:

Craig Laing-*Department of Chemistry, Northwestern University, Evanston, Illinois 60208, USA.* ORCID: 0000-0002-0654-4741

Vinayak P. Dravid- *Department of Electrical and Computer Engineering, Northwestern University, Evanston, Illinois 60208, United States* ORCID: 0000-0002-6007-3063

G. N. Manjunatha Reddy- *University of Lille, CNRS, Centrale Lille, Univ. Artois, UMR 8181 – UCCS – Unité de Catalyse et Chimie du Solide, F-59000 Lille, France.* ORCID: 0000-0002-6007-3063

Can Li- *State Key Laboratory of Catalysis, Dalian Institute of Chemical Physics, Chinese concluAcademy of Sciences, Dalian National Laboratory for Clean Energy, 457 Zhongshan Road, Dalian 116023, China* ORCID: 0000-0002-9301-7850

Edward H. Sargent- *Department of Chemistry, Northwestern University, Evanston, Illinois 60208, USA.* ORCID: 0000-0003-0396-6495

Author contributions

P. Fu, M. Quintero & E. Vasileiadou contribute equally to this work.

Competing interests

The authors declare no competing interests.

Acknowledgements

This work was supported by the National Science Foundation under Grant No. DMR-2019444 (IMOD an NSF-STC). This work used the NUFAB facility of Northwestern University's NUANCE Center, which has received support from the SHyNE Resource (NSF ECCS-2025633), the IIN, and Northwestern MRSEC program (NSF DMR-1720139). The MRSEC program (NSF DMR-1720139) at the Materials Research Center, the International Institute for Nanotechnology (IIN), the Keck Foundation, and the State of Illinois through IIN. GNMR gratefully acknowledges financial support from IR INFRANALYTICS FR2054, France, and EU H2020 for conducting the ssNMR experiments. P. Fu acknowledges the financial support from the Chinese Academy of Science as a visiting scholar at Northwestern University, USA.

Supporting Information

The calculated and experimental XRD patterns and detailed single-crystal information. Additional experimental details, materials, and methods; Optical absorption spectra, Transient-state photoluminescence (TRPL) spectra and Energy band level and work function for all compounds; Materials stability of all compounds, XRD patterns for all the films.

Reference

1. Stranks, S. D.; Snaith, H. J., Metal-halide perovskites for photovoltaic and light-emitting devices. *Nat Nanotechnol* **2015,** *10* (5), 391-402.

2. Yuan, M. J.; Quan, L. N.; Comin, R.; Walters, G.; Sabatini, R.; Voznyy, O.; Hoogland, S.; Zhao, Y. B.; Beauregard, E. M.; Kanjanaboos, P.; Lu, Z. H.; Kim, D. H.; Sargent, E. H., Perovskite energy funnels for efficient light-emitting diodes. *Nat Nanotechnol* **2016,** *11* (10), 872-+.

3. Yang, W. S.; Park, B. W.; Jung, E. H.; Jeon, N. J.; Kim, Y. C.; Lee, D. U.; Shin, S. S.; Seo, J.; Kim, E. K.; Noh, J. H.; Seok, S. I., Iodide management in formamidinium-lead-halide-based perovskite layers for efficient solar cells. *Science* **2017,** *356* (6345), 1376-+.

4. Correa-Baena, J. P.; Saliba, M.; Buonassisi, T.; Gratzel, M.; Abate, A.; Tress, W.; Hagfeldt, A., Promises and challenges of perovskite solar cells. *Science* **2017,** *358* (6364), 739-744.

5. Kojima, A.; Teshima, K.; Shirai, Y.; Miyasaka, T., Organometal Halide Perovskites as Visible-

Light Sensitizers for Photovoltaic Cells. *J Am Chem Soc* **2009,** *131* (17), 6050-+.
6. Chen, H.; Maxwell, A.; Li, C. W.; Teale, S.; Chen, B.; Zhu, T.; Ugur, E.; Harrison, G.; Grater, L.; Wang, J. K.; Wang, Z. W.; Zeng, L. W.; Park, S. M.; Chen, L.; Serles, P.; Awni, R. A.; Subedi, B.; Zheng, X. P.; Xiao, C. X.; Podraza, N. J.; Filleter, T.; Liu, C.; Yang, Y.; Luther, J. M.; De Wolf, S.; Kanatzidis, M. G.; Yan, Y. F.; Sargent, E. H., Regulating surface potential maximizes voltage in all-perovskite tandems. *Nature*.
7. Sidhik, S.; Wang, Y. F.; De Siena, M.; Asadpour, R.; Torma, A. J.; Terlier, T.; Ho, K.; Li, W. B.; Puthirath, A. B.; Shuai, X. T.; Agrawal, A.; Traore, B.; Jones, M.; Giridharagopal, R.; Ajayan, P. M.; Strzalka, J.; Ginger, D. S.; Katan, C.; Alam, M. A.; Even, J.; Kanatzidis, M. G.; Mohite, A. D., Deterministic fabrication of 3D/2D perovskite bilayer stacks for durable and efficient solar cells. *Science* **2022,** *377* (6613), 1425-1430.
8. Tong, J.; Jiang, Q.; Ferguson, A. J.; Palmstrom, A. F.; Wang, X.; Hao, J.; Dunfield, S. P.; Louks, A. E.; Harvey, S. P.; Li, C.; Lu, H.; France, R. M.; Johnson, S. A.; Zhang, F.; Yang, M.; Geisz, J. F.; McGehee, M. D.; Beard, M. C.; Yan, Y.; Kuciauskas, D.; Berry, J. J.; Zhu, K., - Carrier control in Sn–Pb perovskites via 2D cation engineering for all-perovskite tandem solar cells with improved efficiency and stability. **2022,** - *7* (- 7), - 651.
9. Li, C.; Wang, X.; Bi, E.; Jiang, F.; Park, S. M.; Li, Y.; Chen, L.; Wang, Z.; Zeng, L.; Chen, H.; Liu, Y.; Grice, C. R.; Abudulimu, A.; Chung, J.; Xian, Y.; Zhu, T.; Lai, H.; Chen, B.; Ellingson, R. J.; Fu, F.; Ginger, D. S.; Song, Z.; Sargent, E. H.; Yan, Y., Rational design of Lewis base molecules for stable and efficient inverted perovskite solar cells. *Science* **2023,** *379* (6633), 690-694.
10. Tong, J. H.; Jiang, Q.; Ferguson, A. J.; Palmstrom, A. F.; Wang, X. M.; Hao, J.; Dunfield, S. P.; Louks, A. E.; Harvey, S. P.; Li, C. W.; Lu, H. P.; France, R. M.; Johnson, S. A.; Zhang, F.; Yang, M. J.; Geisz, J. F.; McGehee, M. D.; Beard, M. C.; Yan, Y. F.; Kuciauskas, D.; Berry, J. J.; Zhu, K., Carrier control in Sn-Pb perovskites via 2D cation engineering for all-perovskite tandem solar cells with improved efficiency and stability. *Nat Energy* **2022,** *7* (7), 642-651.
11. Zheng, X.; Li, Z.; Zhang, Y.; Chen, M.; Liu, T.; Xiao, C.; Gao, D.; Patel, J. B.; Kuciauskas, D.; Magomedov, A.; Scheidt, R. A.; Wang, X.; Harvey, S. P.; Dai, Z.; Zhang, C.; Morales, D.; Pruett, H.; Wieliczka, B. M.; Kirmani, A. R.; Padture, N. P.; Graham, K. R.; Yan, Y.; Nazeeruddin, M. K.; McGehee, M. D.; Zhu, Z.; Luther, J. M., Co-deposition of hole-selective contact and absorber for improving the processability of perovskite solar cells. *Nat Energy* **2023**.
12. Kim, J. Y.; Lee, J. W.; Jung, H. S.; Shin, H.; Park, N. G., High-Efficiency Perovskite Solar Cells. *Chem Rev* **2020,** *120* (15), 7867-7918.
13. Park, N. G.; Zhu, K., Scalable fabrication and coating methods for perovskite solar cells and solar modules. *Nat Rev Mater* **2020,** *5* (5), 333-350.
14. Son, D. Y.; Kim, S. G.; Seo, J. Y.; Lee, S. H.; Shin, H.; Lee, D.; Park, N. G., Universal Approach toward Hysteresis-Free Perovskite Solar Cell via Defect Engineering. *J Am Chem Soc* **2018,** *140* (4), 1358-1364.
15. Stoumpos, C. C.; Malliakas, C. D.; Kanatzidis, M. G., Semiconducting Tin and Lead Iodide Perovskites with Organic Cations: Phase Transitions, High Mobilities, and Near-Infrared Photoluminescent Properties. *Inorg Chem* **2013,** *52* (15), 9019-9038.
16. Saparov, B.; Mitzi, D. B., Organic-Inorganic Perovskites: Structural Versatility for Functional Materials Design. *Chem Rev* **2016,** *116* (7), 4558-4596.
17. Ruddlesden, S. N.; Popper, P., New Compounds of the K2nif4 Type. *Acta Crystallogr* **1957,** *10* (8),

538-540.
18. Ruddlesden, S. N.; Popper, P., The Compound Sr3ti2o7 and Its Structure. *Acta Crystallogr* **1958,** *11* (1), 54-55.
19. Mao, L. L.; Ke, W. J.; Pedesseau, L.; Wu, Y. L.; Katan, C.; Even, J.; Wasielewski, M. R.; Stoumpos, C. C.; Kanatzidis, M. G., Hybrid Dion-Jacobson 2D Lead Iodide Perovskites. *J Am Chem Soc* **2018,** *140* (10), 3775-3783.
20. Ke, W. J.; Mao, L. L.; Stoumpos, C. C.; Hoffman, J.; Spanopoulos, I.; Mohite, A. D.; Kanatzidis, M. C., Compositional and Solvent Engineering in Dion-Jacobson 2D Perovskites Boosts Solar Cell Efficiency and Stability. *Adv Energy Mater* **2019,** *9* (10).
21. Kumada, N.; Kinomura, N.; Sleight, A. W., CsLaNb2O7. *Acta Crystallogr C* **1996,** *52*, 1063-1065.
22. Viciu, L.; Liziard, N.; Golub, V.; Kodenkandath, T. A.; Wiley, J. B., Transition-metal Dion-Jacobson layered perovskites, M0.5LaNb2O7. *Mater Res Bull* **2004,** *39* (14-15), 2147-2154.
23. Ahmad, S.; Fu, P.; Yu, S. W.; Yang, Q.; Liu, X.; Wang, X. C.; Wang, X. L.; Guo, X.; Li, C., Dion-Jacobson Phase 2D Layered Perovskites for Solar Cells with Ultrahigh Stability (vol 3, pg 794, 2019). *Joule* **2019,** *3* (3), 889-890.
24. Tsai, H. H.; Nie, W. Y.; Blancon, J. C.; Toumpos, C. C. S.; Asadpour, R.; Harutyunyan, B.; Neukirch, A. J.; Verduzco, R.; Crochet, J. J.; Tretiak, S.; Pedesseau, L.; Even, J.; Alam, M. A.; Gupta, G.; Lou, J.; Ajayan, P. M.; Bedzyk, M. J.; Kanatzidis, M. G.; Mohite, A. D., High-efficiency two-dimensional Ruddlesden-Popper perovskite solar cells. *Nature* **2016,** *536* (7616), 312-+.
25. Li, X. T.; Hoffman, J. M.; Kanatzidis, M. G., The 2D Halide Perovskite Rulebook: How the Spacer Influences Everything from the Structure to Optoelectronic Device Efficiency. *Chem Rev* **2021,** *121* (4), 2230-2291.
26. Ansari, F.; Shirzadi, E.; Salavati-Niasari, M.; LaGrange, T.; Nonomura, K.; Yum, J. H.; Sivula, K.; Zakeeruddin, S. M.; Nazeeruddin, M. K.; Gratzel, M.; Dyson, P. J.; Hagfeldt, A., Passivation Mechanism Exploiting Surface Dipoles Affords High-Performance Perovskite Solar Cells. *J Am Chem Soc* **2020,** *142* (26), 11428-11433.
27. Grancini, G.; Roldan-Carmona, C.; Zimmermann, I.; Mosconi, E.; Lee, X.; Martineau, D.; Narbey, S.; Oswald, F.; De Angelis, F.; Graetzel, M.; Nazeeruddin, M. K., One-Year stable perovskite solar cells by 2D/3D interface engineering. *Nature Communications* **2017,** *8*.
28. Vasileiadou, E. S.; Wang, B.; Spanopoulos, I.; Hadar, I.; Navrotsky, A.; Kanatzidis, M. G., Insight on the Stability of Thick Layers in 2D Ruddlesden-Popper and Dion-Jacobson Lead Iodide Perovskites. *J Am Chem Soc* **2021,** *143* (6), 2523-2536.
29. Katan, C.; Mercier, N.; Even, J., Quantum and Dielectric Confinement Effects in Lower-Dimensional Hybrid Perovskite Semiconductors. *Chem Rev* **2019,** *119* (5), 3140-3192.
30. Duan, M.; Jiang, P.; Li, D.; Hu, Y.; Rong, Y. G.; Han, H. W., Efficient hole-conductor-free printable mesoscopic perovskite solar cells based on hybrid carbon electrodes. *Proc Spie* **2018,** *10529*.
31. Xi, J.; Spanopoulos, I.; Bang, K.; Xu, J.; Dong, H.; Yang, Y. G.; Malliakas, C. D.; Hoffman, J. M.; Kanatzidis, M. G.; Wu, Z. X., Alternative Organic Spacers for More Efficient Perovskite Solar Cells Containing Ruddlesden-Popper Phases. *J Am Chem Soc* **2020,** *142* (46), 19705-19714.
32. Vasileiadou, E. S.; Jiang, X.; Kepenekian, M.; Even, J.; De Siena, M. C.; Klepov, V. V.; Friedrich, D.; Spanopoulos, I.; Tu, Q.; Tajuddin, I. S.; Weiss, E. A.; Kanatzidis, M. G., Thick-Layer Lead Iodide Perovskites with Bifunctional Organic Spacers Allylammonium and Iodopropylammonium Exhibiting Trap-State Emission. *J Am Chem Soc* **2022,** *144* (14), 6390-6409.

33. Dou, L. T.; Wong, A. B.; Yu, Y.; Lai, M. L.; Kornienko, N.; Eaton, S. W.; Fu, A.; Bischak, C. G.; Ma, J.; Ding, T. N.; Ginsberg, N. S.; Wang, L. W.; Alivisatos, A. P.; Yang, P. D., Atomically thin two-dimensional organic-inorganic hybrid perovskites. *Science* **2015,** *349* (6255), 1518-1521.

34. Smith, M. D.; Jaffe, A.; Dohner, E. R.; Lindenberg, A. M.; Karunadasa, H. I., Structural origins of broadband emission from layered Pb-Br hybrid perovskites. *Chem Sci* **2017,** *8* (6), 4497-4504.

35. Vasileiadou, E. S.; Hadar, I.; Kepenekian, M.; Even, J.; Tu, Q.; Malliakas, C. D.; Friedrich, D.; Spanopoulos, I.; Hoffman, J. M.; Dravid, V. P.; Kanatzidis, M. G., Shedding Light on the Stability and Structure-Property Relationships of Two-Dimensional Hybrid Lead Bromide Perovskites. *Chem Mater* **2021,** *33* (13), 5085-5107.

36. Li, L. N.; Liu, X. T.; He, C.; Wang, S. S.; Ji, C. M.; Zhang, X. Y.; Sun, Z. H.; Zhao, S. E.; Hong, M. C.; Luo, J. H., A Potential Sn-Based Hybrid Perovskite Ferroelectric Semiconductor. *J Am Chem Soc* **2020,** *142* (3), 1159-1163.

37. Wang, S. X.; Popovic, J.; Burazer, S.; Portniagin, A.; Liu, F. Z.; Low, K. H.; Duan, Z. H.; Li, Y. X.; Xiong, Y.; Zhu, Y. M.; Kershaw, S. V.; Djurisic, A. B.; Rogach, A. L., Strongly Luminescent Dion-Jacobson Tin Bromide Perovskite Microcrystals Induced by Molecular Proton Donors Chloroform and Dichloromethane. *Adv Funct Mater* **2021,** *31* (28).

38. Febriansyah, B.; Lekina, Y.; Kaur, J.; Hooper, T. J. N.; Harikesh, P. C.; Salim, T.; Lim, M. H.; Koh, T. M.; Chakraborty, S.; Shen, Z. X.; Mathews, N.; England, J., Formation of Corrugated n=1 2D Tin Iodide Perovskites and Their Use as Lead-Free Solar Absorbers. *Acs Nano* **2021,** *15* (4), 6395-6409.

39. Xu, Z. T.; Mitzi, D. B., SnI42--based hybrid perovskites templated by multiple organic cations: Combining organic functionalities through noncovalent interactions. *Chem Mater* **2003,** *15* (19), 3632-3637.

40. Mitzi, D. B.; Dimitrakopoulos, C. D.; Kosbar, L. L., Structurally tailored organic-inorganic perovskites: Optical properties and solution-processed channel materials for thin-film transistors. *Chem Mater* **2001,** *13* (10), 3728-3740.

41. Hao, F.; Stoumpos, C. C.; Chang, R. P.; Kanatzidis, M. G., Anomalous band gap behavior in mixed Sn and Pb perovskites enables broadening of absorption spectrum in solar cells. *J Am Chem Soc* **2014,** *136* (22), 8094-9.

42. Ke, W.; Chen, C.; Spanopoulos, I.; Mao, L.; Hadar, I.; Li, X.; Hoffman, J. M.; Song, Z.; Yan, Y.; Kanatzidis, M. G., Narrow-Bandgap Mixed Lead/Tin-Based 2D Dion-Jacobson Perovskites Boost the Performance of Solar Cells. *J Am Chem Soc* **2020,** *142* (35), 15049-15057.

43. Parida, B.; Yoon, S.; Jeong, S. M.; Cho, J. S.; Kim, J. K.; Kang, D. W., Recent progress on cesium lead/tin halide-based inorganic perovskites for stable and efficient solar cells: A review. *Solar Energy Materials and Solar Cells* **2020,** *204*.

44. Ramirez, D.; Schutt, K.; Wang, Z. P.; Pearson, A. J.; Ruggeri, E.; Snaith, H. J.; Stranks, S. D.; Jaramillo, F., Layered Mixed Tin-Lead Hybrid Perovskite Solar Cells with High Stability. *Acs Energy Lett* **2018,** *3* (9), 2246-2251.

45. Savill, K. J.; Ulatowski, A. M.; Farrar, M. D.; Johnston, M. B.; Snaith, H. J.; Herz, L. M., Impact of Tin Fluoride Additive on the Properties of Mixed Tin-Lead Iodide Perovskite Semiconductors. *Adv Funct Mater* **2020,** *30* (52).

46. Eperon, G. E.; Leijtens, T.; Bush, K. A.; Prasanna, R.; Green, T.; Wang, J. T. W.; McMeekin, D. P.; Volonakis, G.; Milot, R. L.; May, R.; Palmstrom, A.; Slotcavage, D. J.;

Belisle, R. A.; Patel, J. B.; Parrott, E. S.; Sutton, R. J.; Ma, W.; Moghadam, F.; Conings, B.; Babayigit, A.; Boyen, H. G.; Bent, S.; Giustino, F.; Herz, L. M.; Johnston, M. B.; McGehee, M. D.; Snaith, H. J., Perovskite-perovskite tandem photovoltaics with optimized band gaps. *Science* **2016,** *354* (6314), 861-865.

47. Lin, R. X.; Xiao, K.; Qin, Z. Y.; Han, Q. L.; Zhang, C. F.; Wei, M. Y.; Saidaminov, M. I.; Gao, Y.; Xu, J.; Xiao, M.; Li, A. D.; Zhu, J.; Sargent, E. H.; Tan, H. R., Monolithic all-perovskite tandem solar cells with 24.8% efficiency exploiting comproportionation to suppress Sn(II) oxidation in precursor ink. *Nature Energy* **2019,** *4* (10), 864-873.

48. Lin, R. X.; Xu, J.; Wei, M. Y.; Wang, Y. R.; Qin, Z. Y.; Liu, Z.; Wu, J. L.; Xiao, K.; Chen, B.; Park, S. M.; Chen, G.; Atapattu, H. R.; Graham, K. R.; Xu, J.; Zhu, J.; Li, L. D.; Zhang, C. F.; Sargent, E. H.; Tan, H. R., All-perovskite tandem solar cells with improved grain surface passivation. *Nature* **2022,** *603* (7899), 73-+.

49. Tong, J. H.; Song, Z. N.; Kim, D. H.; Chen, X. H.; Chen, C.; Palmstrom, A. F.; Ndione, P. F.; Reese, M. O.; Dunfield, S. P.; Reid, O. G.; Liu, J.; Zhang, F.; Harvey, S. P.; Li, Z.; Christensen, S. T.; Teeter, G.; Zhao, D. W.; Al-Jassim, M. M.; van Hest, M.; Beard, M. C.; Shaheen, S. E.; Berry, J. J.; Yan, Y. F.; Zhu, K., Carrier lifetimes of > 1 mu s in Sn-Pb perovskites enable efficient all-perovskite tandem solar cells. *Science* **2019,** *364* (6439), 475-+.

50. Ke, W. J.; Chen, C.; Spanopoulos, I.; Mao, L. L.; Hadar, I.; Li, X. T.; Hoffman, J. M.; Song, Z. N.; Yan, Y. F.; Kanatzidis, M. G., Narrow-Bandgap Mixed Lead/Tin-Based 2D Dion-Jacobson Perovskites Boost the Performance of Solar Cells. *J Am Chem Soc* **2020,** *142* (35), 15049-15057.

51. Im, J.; Stoumpos, C. C.; Jin, H.; Freeman, A. J.; Kanatzidis, M. G., Antagonism between Spin-Orbit Coupling and Steric Effects Causes Anomalous Band Gap Evolution in the Perovskite Photovoltaic Materials CH3NH3Sn1-xPbxI3. *J Phys Chem Lett* **2015,** *6* (17), 3503-3509.

52. Ke, W. J.; Syanopoulos, I.; Tu, Q.; Hadar, I.; Li, X. T.; Shekhawat, G. S.; Dravid, V. P.; Kanatzidis, M. G., Ethylenediammonium-Based "Hollow" Pb/Sn Perovskites with Ideal Band Gap Yield Solar Cells with Higher Efficiency and Stability. *J Am Chem Soc* **2019,** *141* (21), 8627-8637.

53. Ju, D. X.; Dang, Y. Y.; Zhu, Z. L.; Liu, H. B.; Chueh, C. C.; Li, X. S.; Wang, L.; Hu, X. B.; Jen, A. K. Y.; Tao, X. T., Tunable Band Gap and Long Carrier Recombination Lifetime of Stable Mixed CH3NH3PbxSn1-xBr3 Single Crystals. *Chem Mater* **2018,** *30* (5), 1556-1565.

54. Stoumpos, C. C.; Cao, D. H.; Clark, D. J.; Young, J.; Rondinelli, J. M.; Jang, J. I.; Hupp, J. T.; Kanatzidis, M. G., Ruddlesden-Popper Hybrid Lead Iodide Perovskite 2D Homologous Semiconductors. *Chem Mater* **2016,** *28* (8), 2852-2867.

55. Mao, L. L.; Stoumpos, C. C.; Kanatzidis, M. G., Two-Dimensional Hybrid Halide Perovskites: Principles and Promises. *J Am Chem Soc* **2019,** *141* (3), 1171-1190.

56. Vasileiadou, E. S.; Wang, B.; Spanopoulos, I.; Hadar, I.; Navrotsky, A.; Kanatzidis, M. G., Insight on the Stability of Thick Layers in 2D Ruddlesden-Popper and Dion-Jacobson Lead Iodide Perovskites. *J Am Chem Soc* **2021,** *143* (6), 2523-2536.

57. Marchenko, E. I.; Korolev, V. V.; Mitrofanov, A.; Fateev, S. A.; Goodilin, E. A.; Tarasov, A. B., Layer Shift Factor in Layered Hybrid Perovskites: Univocal Quantitative Descriptor of Composition-Structure-Property Relationships. *Chem Mater* **2021,** *33* (4), 1213-1217.

58. Janiak, C., A critical account on pi-pi stacking in metal complexes with aromatic nitrogen-containing ligands. *J Chem Soc Dalton* **2000,** (21), 3885-3896.

59. Barman, S.; Venkataraman, N. V.; Vasudevan, S.; Seshadri, R., Phase transitions in the anchored organic bilayers of long-chain alkylammonium lead iodides (CnH2n+1NH3)(2)PbI4; n=12, 16, 18. *J*

Phys Chem B **2003,** *107* (8), 1875-1883.

60. Dutta, S. K.; Dutta, A.; Das Adhikari, S.; Pradhan, N., Doping Mn2+ in Single-Crystalline Layered Perovskite Microcrystals. *Acs Energy Lett* **2019,** *4* (1), 343-351.

61. Li, L. N.; Liu, X. T.; Li, Y. B.; Xu, Z. Y.; Wu, Z. Y.; Han, S. G.; Tao, K. W.; Hong, M. C.; Luo, J. H.; Sun, Z. H., Two-Dimensional Hybrid Perovskite-Type Ferroelectric for Highly Polarization-Sensitive Shortwave Photodetection. *J Am Chem Soc* **2019,** *141* (6), 2623-2629.

62. Li, L.; Sun, Z.; Wang, P.; Hu, W.; Wang, S.; Ji, C.; Hong, M.; Luo, J., Tailored Engineering of an Unusual (C4 H9 NH3)2 (CH3 NH3)2 Pb3 Br10 Two-Dimensional Multilayered Perovskite Ferroelectric for a High-Performance Photodetector. *Angew Chem Int Ed Engl* **2017,** *56* (40), 12150-12154.

63. Li, Y. Y.; Zheng, G. L.; Lin, C. K.; Lin, J., Synthesis, structure and optical properties of different dimensional organic-inorganic perovskites. *Solid State Sci* **2007,** *9* (9), 855-861.

64. Lufaso, M. W.; Woodward, P. M., Jahn-Teller distortions, cation ordering and octahedral tilting in perovskites. *Acta Crystallogr B* **2004,** *60*, 10-20.

65. Alonso, J. A.; Martinez-Lope, M. J.; Casais, M. T.; Fernandez-Diaz, M. T., Evolution of the Jahn-Teller distortion of MnO6 octahedra in RMnO3 perovskites (R = Pr, Nd, Dy, Tb, Ho, Er, Y): A neutron diffraction study. *Inorg Chem* **2000,** *39* (5), 917-923.

66. Robinson, K.; Gibbs, G. V.; Ribbe, P. H., Quadriatic Elongation - Quantitative Measure of Distortion in Coordination Polyhedra. *Science* **1971,** *172* (3983), 567-&.

67. Dahlman, C. J.; Kubicki, D. J.; Reddy, G. N. M., Interfaces in metal halide perovskites probed by solid-state NMR spectroscopy. *J Mater Chem A* **2021,** *9* (35), 19206-19244.

68. Kubicki, D. J.; Stranks, S. D.; Grey, C. P.; Emsley, L., NMR spectroscopy probes microstructure, dynamics and doping of metal halide perovskites. *Nat Rev Chem* **2021,** *5* (9), 624-645.

69. Piveteau, L.; Morad, V.; Kovalenko, M. V., Solid-State NMR and NQR Spectroscopy of Lead-Halide Perovskite Materials. *J Am Chem Soc* **2020,** *142* (46), 19413-19437.

70. Dahlman, C. J.; Kennard, R. M.; Paluch, P.; Venkatesan, N. R.; Chabinyc, M. L.; Reddy, G. N. M., Dynamic Motion of Organic Spacer Cations in Ruddlesden-Popper Lead Iodide Perovskites Probed by Solid-State NMR Spectroscopy. *Chem Mater* **2021,** *33* (2), 642-656.

71. Fu, P.; Quintero, M. A.; Welton, C.; Li, X. T.; Cucco, B.; De Siena, M. C.; Even, J.; Volonakis, G.; Kepenekian, M.; Liu, R. Z.; Laing, C. C.; Klepov, V.; Liu, Y. K.; Dravid, V. P.; Reddy, G. N. M.; Li, C.; Kanatzidis, M. G., Short Aromatic Diammonium Ions Modulate Distortions in 2D Lead Bromide Perovskites for Tunable White-Light Emission. *Chem Mater* **2022,** *34* (21), 9685-9698.

72. Raval, P.; Akhavan Kazemi, M. A.; Ruellou, J.; Trébosc, J.; Lafon, O.; Delevoye, L.; Sauvage, F.; Manjunatha Reddy, G. N., Examining a Year-Long Chemical Degradation Process and Reaction Kinetics in Pristine and Defect-Passivated Lead Halide Perovskites. *Chem Mater* **2023,** *35* (7), 2904-2917.

73. Rosales, B.; Men, L.; Cady, S.; Hanrahan, M.; Rossini, A.; Vela, J., Persistent dopants and phase segregation in organolead mixed-halide perovskites. *Abstr Pap Am Chem S* **2018,** *255*.

74. Lee, J.; Lee, W.; Kang, K.; Lee, T.; Lee, S. K., Layer-by-Layer Structural Identification of 2D Ruddlesden-Popper Hybrid Lead Iodide Perovskites by Solid-State NMR Spectroscopy. *Chem Mater* **2021,** *33* (1), 370-377.

75. Raval, P.; Kennard, R. M.; Vasileiadou, E. S.; Dahlman, C. J.; Spanopoulos, I.; Chabinyc, M. L.; Kanatzidis, M.; Reddy, G. N. M., Understanding Instability in Formamidinium Lead Halide

Perovskites: Kinetics of Transformative Reactions at Grain and Subgrain Boundaries. *Acs Energy Lett* **2022,** *7* (4), 1534-1543.

76. Yamada, K.; Fujise, K.; Hino, S.; Yamane, Y.; Nakagama, T., Characterization of Sn(II)-based Perovskites by XRD, DTA, NQR and Sn-119 NMR for Photovoltaic Applications. *Chem Lett* **2019,** *48* (7), 749-752.

77. Kubicki, D. J.; Prochowicz, D.; Salager, E.; Rakhmatullin, A.; Grey, C. P.; Emsley, L.; Stranks, S. D., Local Structure and Dynamics in Methylammonium, Formamidinium, and Cesium Tin(II) Mixed-Halide Perovskites from Sn-119 Solid-State NMR. *J Am Chem Soc* **2020,** *142* (17), 7813-7826.

78. Karmakar, A.; Bhattacharya, A.; Sarkar, D.; Bernard, G. M.; Mar, A.; Michaelis, V. K., Influence of hidden halogen mobility on local structure of CsSn(Cl1-xBrx)(3) mixed-halide perovskites by solid-state NMR. *Chem Sci* **2021,** *12* (9), 3253-3263.

79. Krishna, A.; Zhang, H.; Zhou, Z.; Gallet, T.; Dankl, M.; Ouellette, O.; Eickemeyer, F. T.; Fu, F.; Sanchez, S.; Mensi, M.; Zakeeruddin, S. M.; Rothlisberger, U.; Manjunatha Reddy, G. N.; Redinger, A.; Gratzel, M.; Hagfeldt, A., Nanoscale interfacial engineering enables highly stable and efficient perovskite photovoltaics. *Energy Environ Sci* **2021,** *14* (10), 5552-5562.

80. Knutson, J. L.; Martin, J. D.; Mitzi, D. B., Tuning the band gap in hybrid tin iodide perovskite semiconductors using structural templating. *Inorg Chem* **2005,** *44* (13), 4699-4705.

81. Pedesseau, L.; Sapori, D.; Traore, B.; Robles, R.; Fang, H. H.; Loi, M. A.; Tsai, H. H.; Nie, W. Y.; Blancon, J. C.; Neukirch, A.; Tretiak, S.; Mohite, A. D.; Katan, C.; Even, J.; Kepenekian, M., Advances and Promises of Layered Halide Hybrid Perovskite Semiconductors. *Acs Nano* **2016,** *10* (11), 9776-9786.

82. Gong, X. W.; Voznyy, O.; Jain, A.; Liu, W. J.; Sabatini, R.; Piontkowski, Z.; Walters, G.; Bappi, G.; Nokhrin, S.; Bushuyev, O.; Yuan, M. J.; Comin, R.; McCamant, D.; Kelley, S. O.; Sargent, E. H., Electron-phonon interaction in efficient perovskite blue emitters. *Nat Mater* **2018,** *17* (6), 550-+.

83. Neaton, J. B.; Ederer, C.; Waghmare, U. V.; Spaldin, N. A.; Rabe, K. M., First-principles study of spontaneous polarization in multiferroic BiFeO3. *Phys Rev B* **2005,** *71* (1).

84. Hao, F.; Stoumpos, C. C.; Chang, R. P. H.; Kanatzidis, M. G., Anomalous Band Gap Behavior in Mixed Sn and Pb Perovskites Enables Broadening of Absorption Spectrum in Solar Cells. *J Am Chem Soc* **2014,** *136* (22), 8094-8099.

85. Wang, N. N.; Cheng, L.; Ge, R.; Zhang, S. T.; Miao, Y. F.; Zou, W.; Yi, C.; Sun, Y.; Cao, Y.; Yang, R.; Wei, Y. Q.; Guo, Q.; Ke, Y.; Yu, M. T.; Jin, Y. Z.; Liu, Y.; Ding, Q. Q.; Di, D. W.; Yang, L.; Xing, G. C.; Tian, H.; Jin, C. H.; Gao, F.; Friend, R. H.; Wang, J. P.; Huang, W., Perovskite light-emitting diodes based on solution-processed self-organized multiple quantum wells. *Nat Photonics* **2016,** *10* (11), 699-+.

86. Sun, Y.; Zhang, L.; Wang, N. N.; Zhang, S. T.; Cao, Y.; Miao, Y. F.; Xu, M. M.; Zhang, H.; Li, H.; Yi, C.; Wang, J. P.; Huang, W., The formation of perovskite multiple quantum well structures for high performance light-emitting diodes. *Npj Flex Electron* **2018,** *2* (1).

87. Mao, L. L.; Guo, P. J.; Kepenekian, M.; Hadar, I.; Katan, C.; Even, J.; Schaller, R. D.; Stoumpos, C. C.; Kanatzidis, M. G., Structural Diversity in White-Light-Emitting Hybrid Lead Bromide Perovskites. *J Am Chem Soc* **2018,** *140* (40), 13078-13088.

88. Rajagopal, A.; Stoddard, R. J.; Hillhouse, H. W.; Jen, A. K. Y., On understanding bandgap bowing and optoelectronic quality in Pb-Sn alloy hybrid perovskites. *J Mater Chem A* **2019,** *7* (27), 16285-16293.

89. Harris, R. K.; Becker, E. D.; De Menezes, S. M. C.; Goodfellow, R.; Granger, P., NMR nomenclature. Nuclear spin properties and conventions for chemical shifts - (IUPAC recommendations 2001). *Pure Appl Chem* **2001,** *73* (11), 1795-1818.

Table 1. Crystal data and structure refinement for $(BA)_2(MA)_{n-1}Pb_xSn_{n-x}Br_{3n+1}$ (n = 1−3) and $(3AMPY)(MA)_{n-1}Pb_xSn_{n-x}Br_{3n+1}$ (n = 1−3) at 293 K.

Compound	$(BA)_2Pb_{0.83}Sn_{0.17}Br_4$	$(BA)_2MAPb_{1.31}Sn_{0.69}Br_7$	$(BA)_2MA_2Pb_{2.02}Sn_{0.98}Br_{10}$
Empirical formula	C8H20Br4N2Pb0.83Sn0.17	C9H25Br7N3Pb1.31Sn0.69	C10H36Br10N4Pb2.02Sn0.98
Formula weight	656.49	1088.00	1546.14
Crystal system	orthorhombic	orthorhombic	orthorhombic
Space group	Cmc21	Pbcn	Cmc21
Unit cell dimensions	a = 27.641(6) Å, α = 90° b = 8.3381(17) Å, β = 90° c = 8.2230(16) Å, γ = 90°	a = 39.1754(17) Å, α = 90° b = 8.3831(3) Å, β = 90° c = 8.2683(3) Å, γ = 90°	a = 51.082(3) Å, α = 90° b = 8.3679(4) Å, β = 90° c = 8.2930(4) Å, γ = 90°
Volume	1895.2(7) $Å^3$	2715.40(18) $Å^3$	3544.8(3) $Å^3$
Z	4	4	4
Density (calculated)	2.301 g/cm^3	2.661 g/cm^3	2.897 g/cm^3
Absorption coefficient	16.070 mm^{-1}	10.232 mm^{-1}	21.524 mm^{-1}
Index ranges	-38<=h<=38, -11<=k<=11, -11<=l<=10	-58<=h<=58, -12<=k<=12, -11<=l<=12	-72<=h<=77, -12<=k<=11, -12<=l<=10
Reflections collected	7243	20923	19722
Independent reflections	2566 [R_{int} = 0.0424]	4833 [R_{int} = 0.0352]	5729 [R_{int} = 0.0387]
Completeness	99.8%	98.5%	99.9%
Data / restraints / parameters	2566 / 22 / 77	4833 / 34 / 102	5729 / 30 / 116
Goodness-of-fit	1.050	1.130	1.032
Final R indices [I > 2σ(I)]	R_{obs} = 0.0586, wR_{obs} = 0.1588	R_{obs} = 0.0900, wR_{obs} = 0.2158	R_{obs} = 0.0479, wR_{obs} = 0.1098
R indices [all data]	R_{all} = 0.0838, wR_{all} = 0.1799	R_{all} = 0.1203, wR_{all} = 0.2336	R_{all} = 0.0799, wR_{all} = 0.1216
Largest diff. peak and hole	2.459 and -3.228 e·$Å^{-3}$	1.650 and -2.226 e·$Å^{-3}$	2.263 and -0.843 e·$Å^{-3}$
Compound	$(3AMP)Pb_{0.79}Sn_{0.21}Br_4$	$(3AMP)MAPb_{1.44}Sn_{0.56}Br_7$	$(3AMP)MA_2Pb_{1.56}Sn_{1.44}Br_{10}$
Empirical formula	C6H10Br4N2Pb0.79 Sn0.21	C7H16Br7N3Pb1.44Sn0.56	C8 H22 Br10 N4 Pb1.56 Sn1.44
Formula weight	618.18	1066.42	1467.75
Crystal system	Triclinic	Monoclinic	Monoclinic
Space group	$P\bar{1}$	$P2_1/c$	Cc
Unit cell dimensions	a = 10.614(2) Å, α = 86.72(3)° b = 11.851(2) Å,	a = 15.568(3) Å, α = 90° b = 17.165(3) Å,	a = 42.906(9) Å, α = 90° b = 8.5286(17) Å,

	β = 64.57(3)°	β = 97.23(3)°	β = 95.82(3)°
	c = 11.896(2) Å,	c = 8.2140(16) Å,	c = 8.2673(17) Å,
	γ = 81.14(3)°	γ = 90°	γ = 90°
Volume	1335.2(6) $Å^3$	2177.5(8) $Å^3$	3009.6(11) $Å^3$
Z	4	4	4
Density (calculated)	3.075 g/cm^3	3.253 g/cm^3	3.239 g/cm^3
Absorption coefficient	11.984 mm^{-1}	13.223 mm^{-1}	12.439 mm^{-1}
Index ranges	-14<=h<=14, -15<=k<=16, -16<=l<=16	-19<=h<=19, -21<=k<=21, -10<=l<=10	-72<=h<=70, -14<=k<=13, -12<=l<=14
Reflections collected	25517	14407	18244
Independent reflections	7087 [R_{int} = 0.0312]	4561 [R_{int} = 0.0786]	9868 [R_{int} = 0.0813]
Completeness	99.6%	96.2%	99.6%
Data / restraints / parameters	7087 / 2 / 239	4561 / 5 / 132	9868 / 33 / 175
Goodness-of-fit	0.665	0.905	0.634
Final R indices [I > 2σ(I)]	R_{obs} = 0.0253, wR_{obs} = 0.0391	R_{obs} = 0.0660, wR_{obs} = 0.1713	R_{obs} = 0.0870, wR_{obs} = 0.2005
R indices [all data]	R_{all} = 0.0484, wR_{all} = 0.0403	R_{all} = 0.1083, wR_{all} = 0.1928	R_{all} = 0.2011, wR_{all} = 0.2170
Largest diff. peak and hole	1.697 and -0.880 e·$Å^{-3}$	4.175 and -2.329 e·$Å^{-3}$	11.722 and -2.398 e·$Å^{-3}$

$R = \Sigma||F_o|-|F_c|| / \Sigma|F_o|$, $wR = [\Sigma[w(|F_o|^2 - |F_c|^2)^2] / \Sigma[w(|F_o|^4)]]$

Table 2. Crystal data comparison for $(BA)_2(MA)_{n-1}Pb_xSn_{n-x}Br_{3n+1}$ (n = 1−3), pure lead $(BA)_2$ $(MA)_{n-1}Pb_nBr_{3n+1}$ (n = 1−3) and pure tin $(BA)_2$ $(MA)_{n-1}Sn_nBr_{3n+1}$ (n = 1−3) compounds.

Compound	Structure	Space group	Unit cell		V (Å^3)	Bond Angle variance (deg^2)	Bond length distortion
$(BA)_2PbBr_4$[60]	2D (n=1)	Pbca	a = 8.25460 Å b = 8.14220 Å c = 27.46310 Å	α = 90° β = 90° γ = 90°	1845.8116	8.5419	0.00509
$(BA)_2Pb_{0.83}Sn_{0.17}Br_4$ This work	2D (n=1)	Cmc21	a = 27.641(6) Å, b = 8.3381(17) Å, c = 8.2230(16) Å,	α = 90° β = 90° γ = 90°	1895.2(7)	0.3401	0.0041
$(BA)_2SnBr_6$	0D	P 21	a = 10.34200 Å b = 7.67800 Å c = 12.51700 Å	α = 90° β = 103.23° γ = 90°	967.5438	1.3323	0.00467
$(BA)_2MAPb_2Br_7$[61]	2D (n=2)	Cmc21	a = 39.13580 Å b = 8.34630 Å c = 8.18040 Å	α = 90° β = 90° γ = 90°	2672.0387	20.1010	0.01070
$(BA)_2MAPb_{1.31}Sn_{0.69}Br_7$ This work	2D (n=2)	Pbcn	a = 39.1754(17) Å, b = 8.3831(3) Å, c = 8.2683(3) Å,	α = 90° β = 90° γ = 90°	2715.40(18)	9.7383	0.0131
$(BA)_2MA_2Pb_3Br_{10}$[62]	2D (n=3)	Cmc21	a = 51.02100 Å b = 8.37830 Å c = 8.28740 Å	α = 90° β = 90° γ = 90°	3608.9314	1.5038	0.00762
$(BA)_2MA_2Pb_{2.02}Sn_{0.98}Br_{10}$ This work	2D (n=3)	Cmc21	a = 51.082(3) Å, b = 8.3679(4) Å, c = 8.2930(4) Å,	α = 90° β = 90° γ = 90°	3544.8(3)	12.7891	0.0188
$(BA)_2MA_2Sn_3Br_{10}$[36]	2D (n=3)	Cmc21	a = 51.02100 Å b = 8.37830 Å c = 8.28740 Å	α = 90° β = 90° γ = 90°	3542.6086	14.3106	0.02546
$(3AMPY)PbBr_6$[63]	0D	Pbca	a = 15.78800 Å b = 8.14600 Å c = 17.21500 Å	α = 90° β = 90° γ = 90°	2214.0048	5.2751	0.00463
$(3AMPY)Pb_{0.79}Sn_{0.21}Br_4$ This work	2D (n=1)	P $\bar{1}$	a = 10.614(2) Å, b = 11.851(2) Å, c = 11.896(2) Å,	α = 86.72(3)° β = 64.57(3)° γ = 81.14(3)°	1335.2(6)	35.907	0.0115
$(3AMPY)SnBr_4$ This work	2D (n=1)	P 1	a = 10.717(2) Å, b = 11.811(2) Å, c = 11.833(2) Å,	α = 85.04(3)° β = 63.76(3)° γ = 80.94(3)°	1326.45(6)	34.762	0.0465

Table 3. Comparison of Pb/Sn−Br−Pb/Sn Angles, d-Spacing, bond length distortion, and bond angle variance for $(BA)_2(MA)_{n-1}Pb_xSn_{n-x}Br_{3n+1}$ (n = 1−3) and $(3AMPY)(MA)_{n-1}Pb_xSn_{n-x}Br_{3n+1}$ (n = 1−3), respectively.

Compound	Axial Pb/Sn-Br-Pb/Sn angle (deg)	Equatorial Pb/Sn-Br-Pb/Sn angle (deg)	Average Pb/Sn-Br-Pb/Sn angle (deg)	Adjacent Br-Br Distance (Å)	Stacking Axis (Å)	Bond angle variance (deg^2)	Bond length distortion	Shift factor
$(BA)_2Pb_{0.83}Sn_{0.17}Br_4$ (n=1)		155.8(3)		8.886(6)	20.227(7)	0.3401	0.0041	(0,0)
$(BA)_2MAPb_{1.31}Sn_{0.69}Br_7$ (n=2)	179.93(10)	163.09(10)	171.51(10)	8.786(4)	31.732(5)	9.7383	0.0131	(0.12,0.12)
$(BA)_2MA_2Pb_{2.02}Sn_{0.98}Br_{10}$ (n=3)	175.25(14)	170.85(10)	173.05(12)	8.833(3)	43.505(4)	12.7891	0.0188	(0.25,0.25)
$(3AMPY)Pb_{0.79}Sn_{0.21}Br_4$ (n=1)		162.42(3)		5.9926(17)	16.106(4)	35.907	0.0115	(0.12,0.12)
$(3AMPY)MAPb_{1.44}Sn_{0.56}Br_7$ (n=2)	170.02(12)	167.49(7)	168.76	4.252(4)	27.276(4)	11.0041	0.0110	(0.15,0.15)
$(3AMPY)MA_2Pb_{1.56}Sn_{1.44}Br_{10}$ (n=3)	171.40(4)	171.40(4)	171.40(4)	4.196(12)	39.051(15)	7.881	0.0138	(0.5,0.5)

Table 4. Optical band-gaps, energy at maximum PL, full width at half maximum of PL, and average effective mass of the compounds calculated based on the for $(BA)_2(MA)_{n-1}Pb_xSn_{n-x}Br_{3n+1}$ (n = 1−3) and $(3AMPY)(MA)_{n-1}Pb_xSn_{n-x}Br_{3n+1}$ (n = 1−3), respectively.

Compound	Band gap E_g (eV)	Excitonic absorption (eV)	PL(eV)	FWHW eV (nm)	Color
$(BA)_2Pb_{0.8}Sn_{0.2}Br_4$ (n=1)	2.47	3.19	3.02	0.08(10.81)	yellow
$(BA)_2MAPb_{1.3}Sn_{0.7}Br_7$ (n=2)	2.15	3.02	2.84	0.11(37.52)	Light orange
$(BA)_2MA_2Pb_{1.9}Sn_{1.1}Br_{10}$ (n=3)	1.97	2.77	2.48	0.19(37.52)	Dark Orange
$(3AMPY)Pb_{0.8}Sn_{0.2}Br_4$ (n=1)	2.41	2.94	2.56	0.23(43.43)	Light orange
$(3AMPY)MAPb_{1.5}Sn_{0.5}Br_7$ (n=2)	2.17	2.78	2.47	0.18(36.63)	Light red
$(3AMPY)MA_2Pb_{1.7}Sn_{1.3}Br_{10}$ (n=3)	1.86	2.95	2.36	0.16(35.36)	Red
$(BA)_2PbBr_4$ (n=1)	2.92	3.19 (SI)	2.92[82]	0.22(29.56)	White
$(BA)_2MAPb_2Br_7$[35] (n=2)	2.68	2.81	2.58[61]	0.26(57.09)	Yellow
$(BA)_2MA_2Pb_3Br_{10}$ (n=3)	2.57	2.94	2.50	0.09(15.70)	Orange
$(BA)_2SnBr_4$ (n=1)	3.44		2.36		
$(BA)_2MASn_2Br_7$ (n=2)	2.27		2.82		Yellow
$(BA)_2MA_2Sn_3Br_{10}$ (n=3)	2.22		2.71		Orange

Table 5. Summary of PL average lifetimes for 2D $(BA)_2(MA)_{n-1}Pb_xSn_{n-x}Br_{3n+1}$ (n = 1−3) and (3AMPY)$(MA)_{n-1}Pb_xSn_{n-x}$ Br_{3n+1} (n = 1−3) compounds, respectively.

Compound	τ_1	τ_2	τ_3	$\tau_{average}$
$(BA)_2Pb_{0.83}Sn_{0.17}Br_4$	0.91 (39.39%)	2.98 (53.12%)	11.20 (7.48%)	2.78 ns
$(BA)_2MAPb_{1.31}Sn_{0.69}Br_7$	0.93 (41.90%)	3.19 (51.40%)	12.66 (7.70%)	3.32 ns
$(BA)_2MA_2Pb_{2.02}Sn_{0.98}Br_{10}$	0.86 (22.25%)	3.51 (61.86%)	14.08 (15.89%)	4.77 ns
$(3AMPY)Pb_{0.79}Sn_{0.21}Br_4$	0.87 (16.58%)	5.25 (38.12%)	17.89 (45.31%)	10.25 ns
$(3AMPY)MAPb_{1.44}Sn_{0.56}Br_7$	0.91 (13.24%)	5.02 (39.36%)	25.28 (47.39%)	14.07 ns
$(3AMPY)MA_2Pb_{1.56}Sn_{1.44}Br_{10}$	1.01 (6.11%)	5.57 (23.45%)	24.74 (70.44%)	18.80 ns

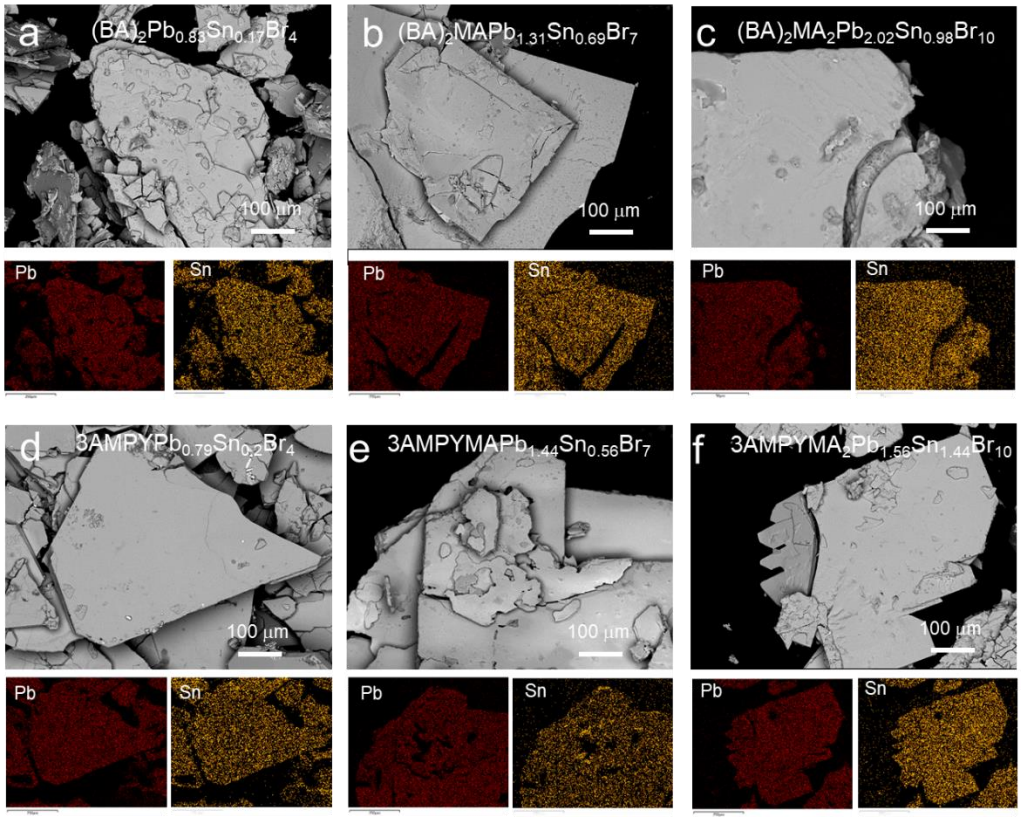

Figure 2. Overall microstructure and composition analyses: Scanning Electron Microscopy/Energy Dispersive X-ray Spectrometry (SEM/EDS) of (a-c) $(BA)_2(MA)_{n-1}$

$Pb_xSn_{n-x}Br_{3n+1}$ (n = 1−3) and (d-f) (3AMPY) $(MA)_{n-1}Pb_xSn_{n-x}Br_{3n+1}$ (n = 1−3) series compounds, respectively.

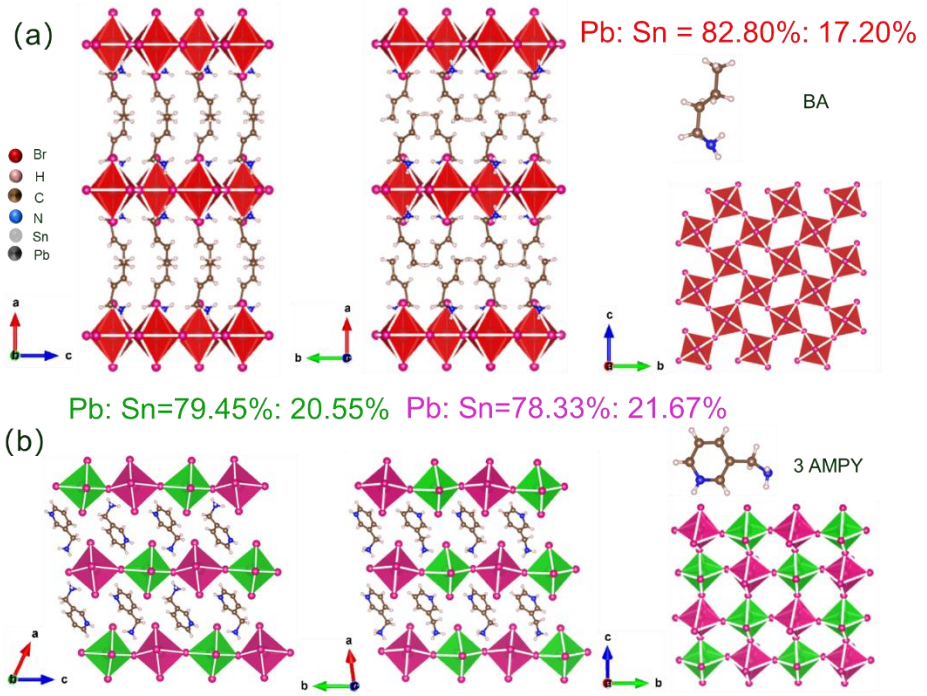

Figure 3. Comparative view of the crystal structures for (a) the $(BA)_2(Pb_{0.83}Sn_{0.17})Br_4$ (n = 1, x= 0.83) and (b) $(3AMPY)Pb_{0.79}Sn_{0.21}Br_4$ (n = 1, x= 0.79), respectively.

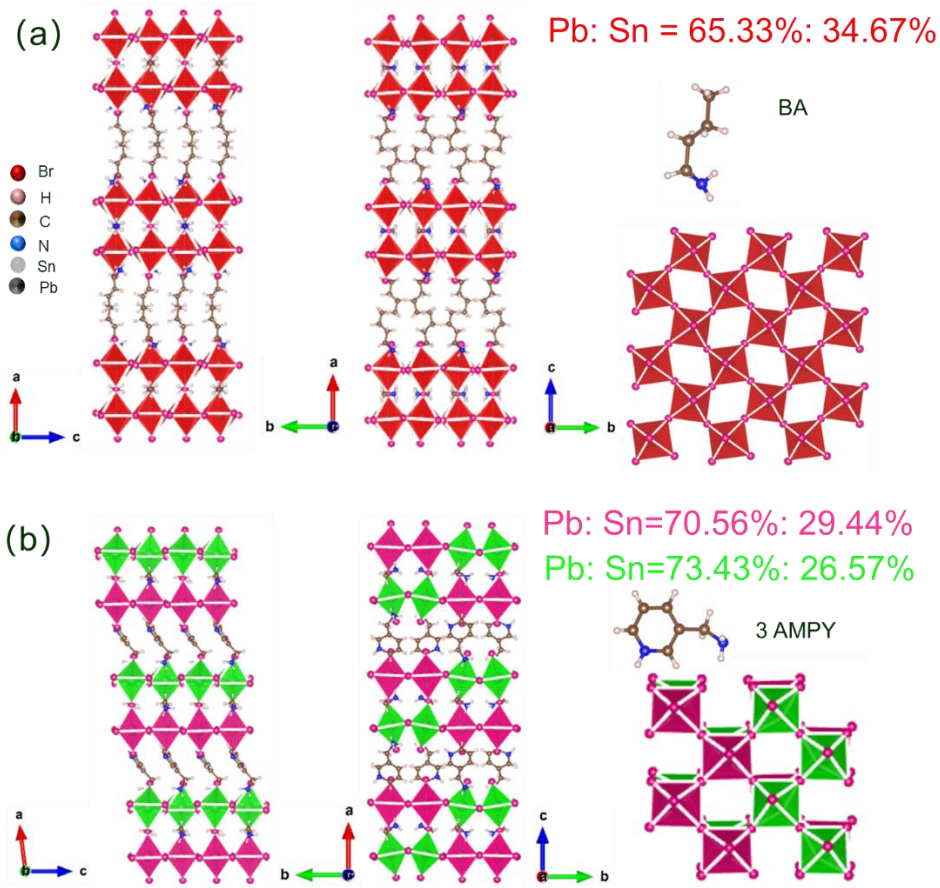

Figure 4. Comparative view of the crystal structures for (a) the $(BA)_2(MA)(Pb_{1.31}Sn_{0.69})_2Br_7$ (n = 2, x= 1.31) and (b) $(3AMPY)(MA)(Pb_{1.44}Sn_{0.56})_2Br_7$ (n = 2, x= 1.44), respectively.

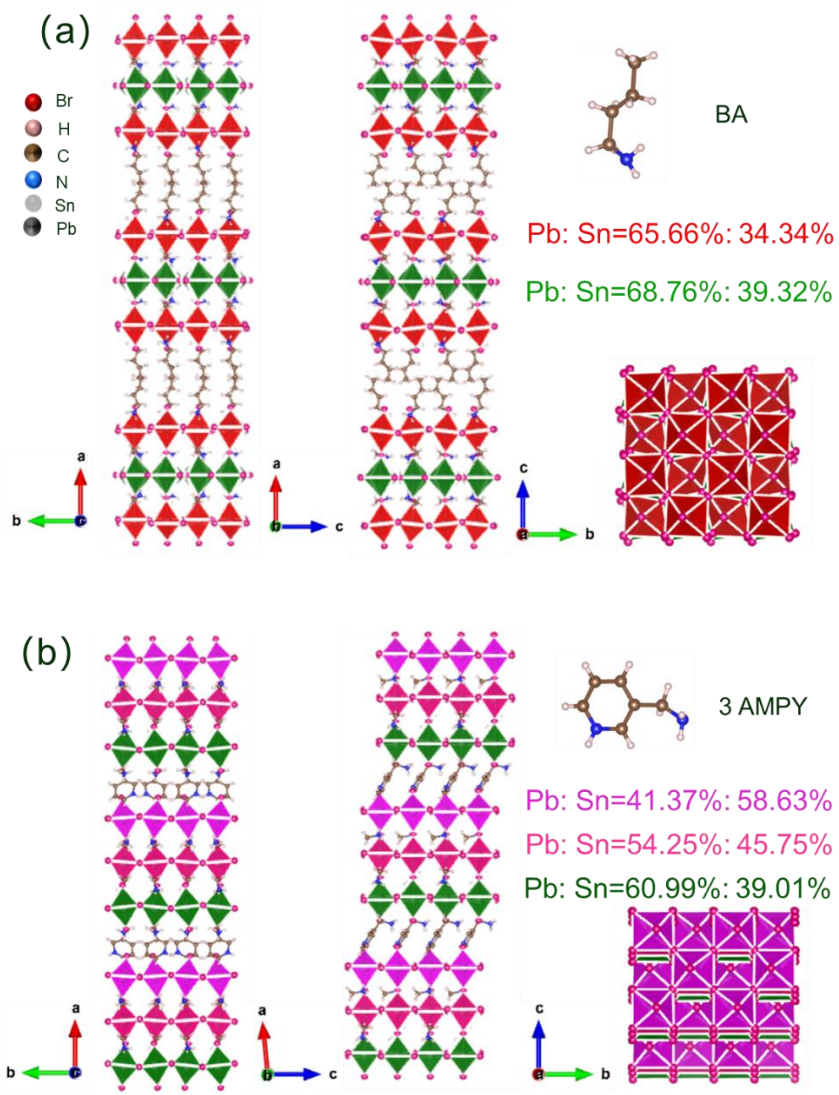

Figure 5. Comparative view of the crystal structures for (a) the $(BA)_2(MA)_2(Pb_{2.02}Sn_{0.98})_3Br_{10}$ (n = 3, x= 2.02) and (b) $(3AMPY)(MA)_2(Pb_{1.56}Sn_{1.44})_3Br_{10}$ (n = 3, x= 1.56), respectively.

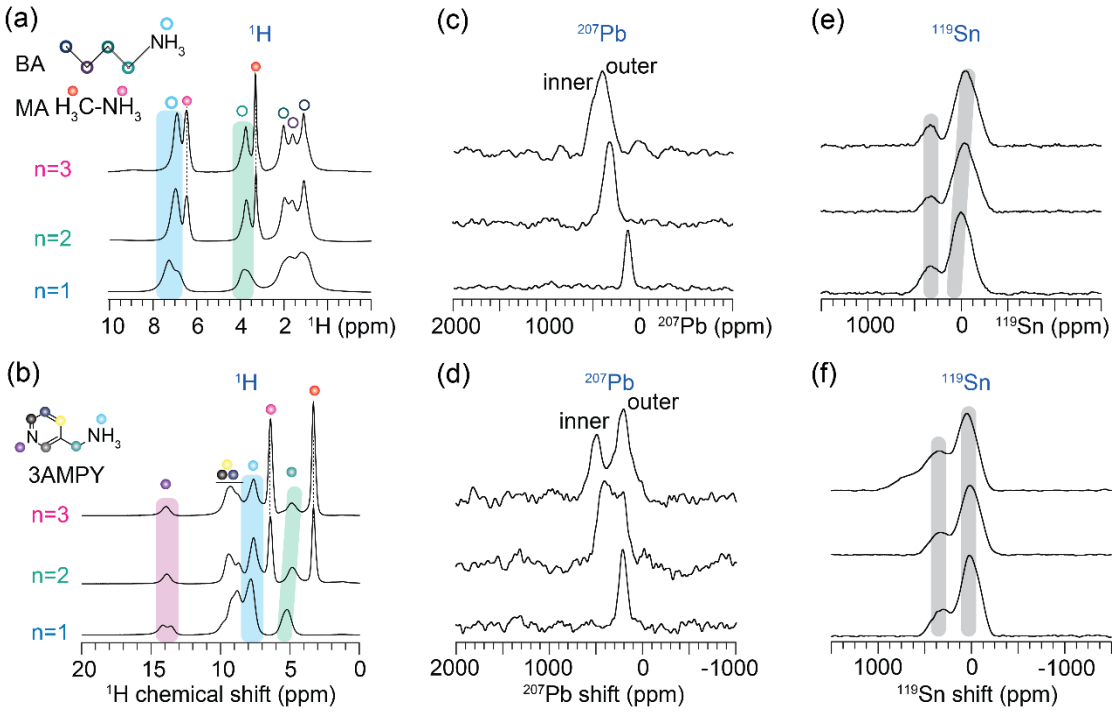

Figure 6. Solid-state 1D (a,b) ^{1}H MAS, (c,d) ^{207}Pb MAS and (e,f) ^{119}Sn MAS NMR spectra of $(BA)_2(MA)_{n-1}Pb_{nx}Sn_{n-nx}Br_{3n+1}$ (n = 1−3) RP phases on top panels, and for $(3AMPY)(MA)_{n-1}Pb_{nx}Sn_{n-nx}Br_{3n+1}$ (n = 1−3) in the lower panels. All spectra were acquired at 18.8 T (^{1}H = 800 MHz) and 50 kHz MAS. The vertical bands indicate the changes in chemical shifts across n=1-3 layered structures.

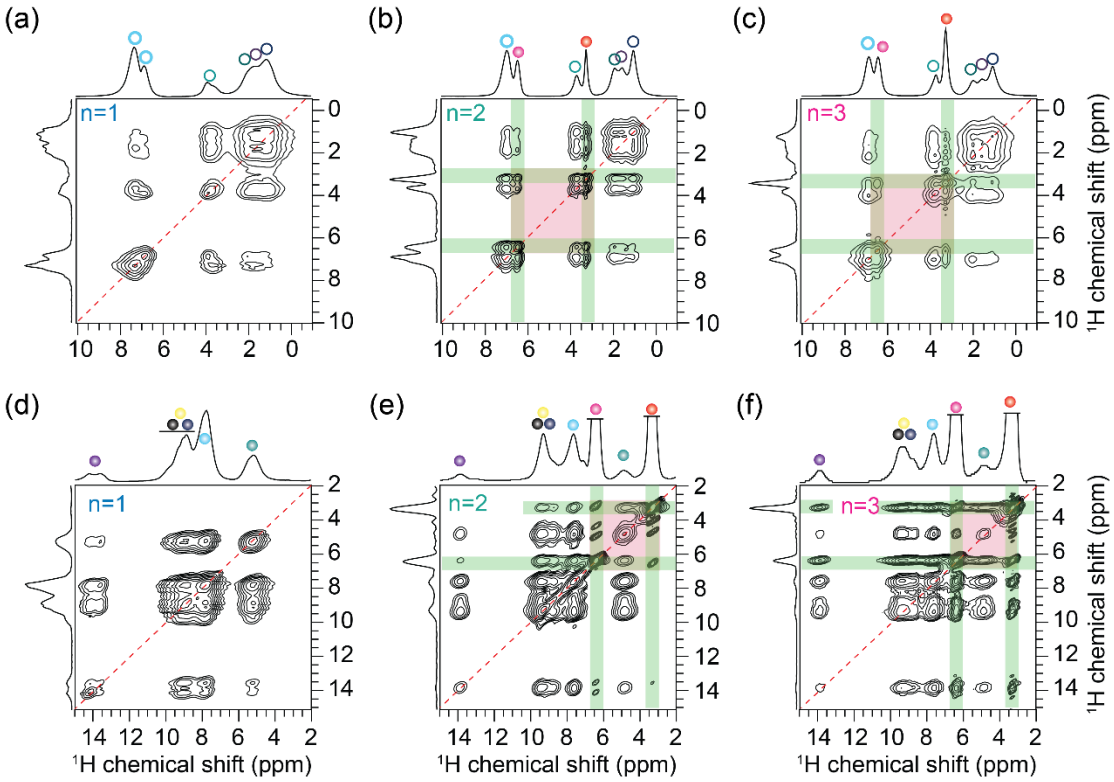

Figure 7. 2D ^{1}H-^{1}H spin diffusion spectrum of $(BA)_2(MA)_{n-1}Pb_{nx}Sn_{n-nx}Br_{3n+1}$ (a) n=1 (b) n=2 (c) n=3 and $(3AMPY)(MA)_{n-1}Pb_{nx}Sn_{n-nx}Br_{3n+1}$ (d) n=1 (e) n=2 and (f) n=3. All spectra were acquired at 18.8 T (^{1}H = 800 MHz) and 50 kHz MAS, and with 500 ms of mixing time. The magenta boxes indicate the peaks correspond to the MA cations, and the horizontal and vertical green bands depict the through space proximity between the large spacer cations and the MA cations.

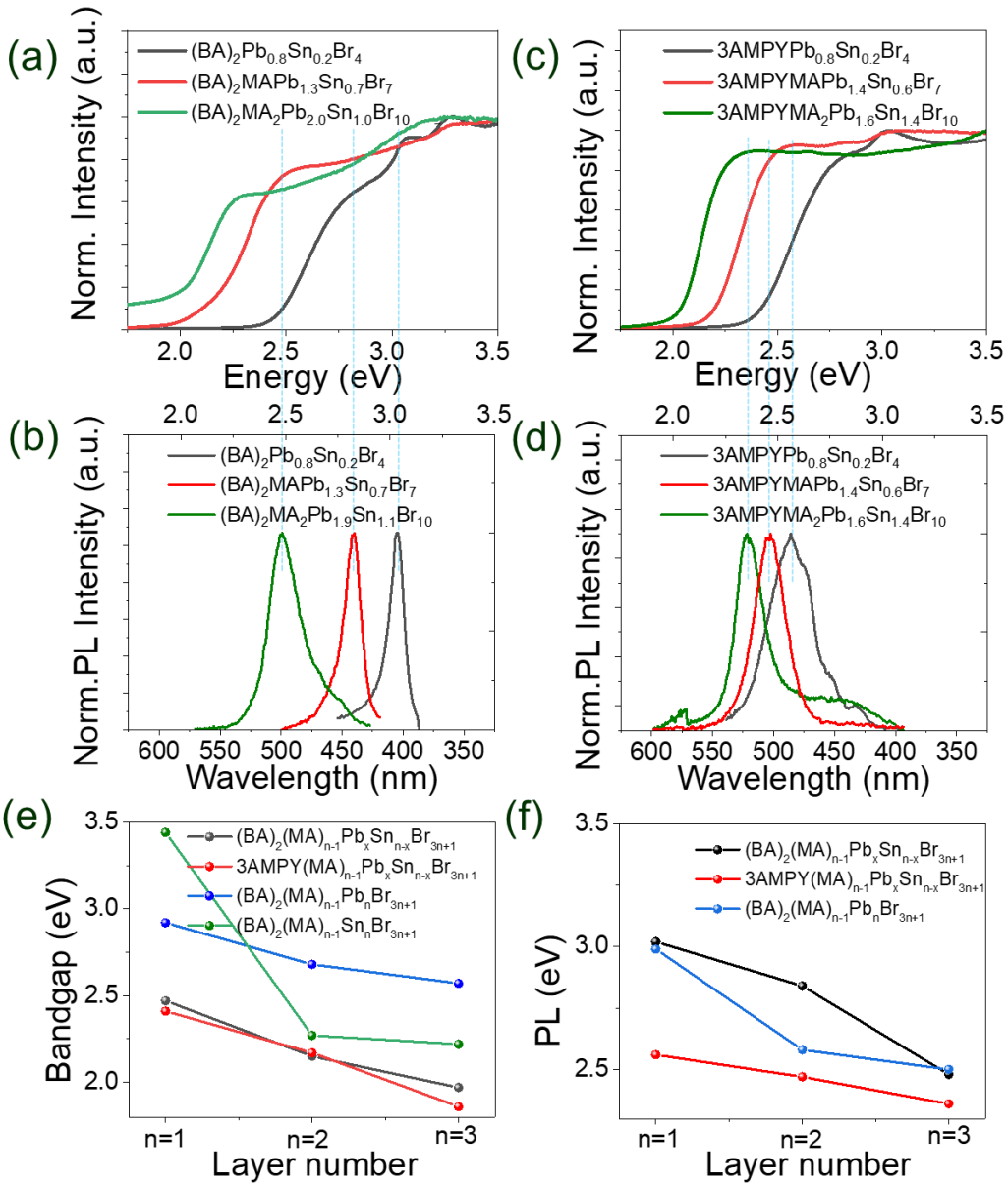

Figure 8. Optical absorption and steady-state photoluminescence (PL) spectra for (a, b) $(BA)_2(MA)_{n-1}Pb_xSn_{n-x}Br_{3n+1}$, (c, d) $3AMPY(MA)_{n-1}Pb_xSn_{n-x}Br_{3n+1}$ (n = 1−3) series and (e, f) optical bandgap values extrapolated from the edge of the absorption spectra and positions of the maxima of the PL spectra for the corresponding $(BA)_2(MA)_{n-1}Pb_xSn_{n-x}Br_{3n+1}$ series, pure tin $(BA)_2(MA)_{n-1}Sn_nBr_{3n+1}$ compounds and pure lead $(BA)_2(MA)_{n-1}Pb_nBr_{3n+1}$ compounds, respectively.

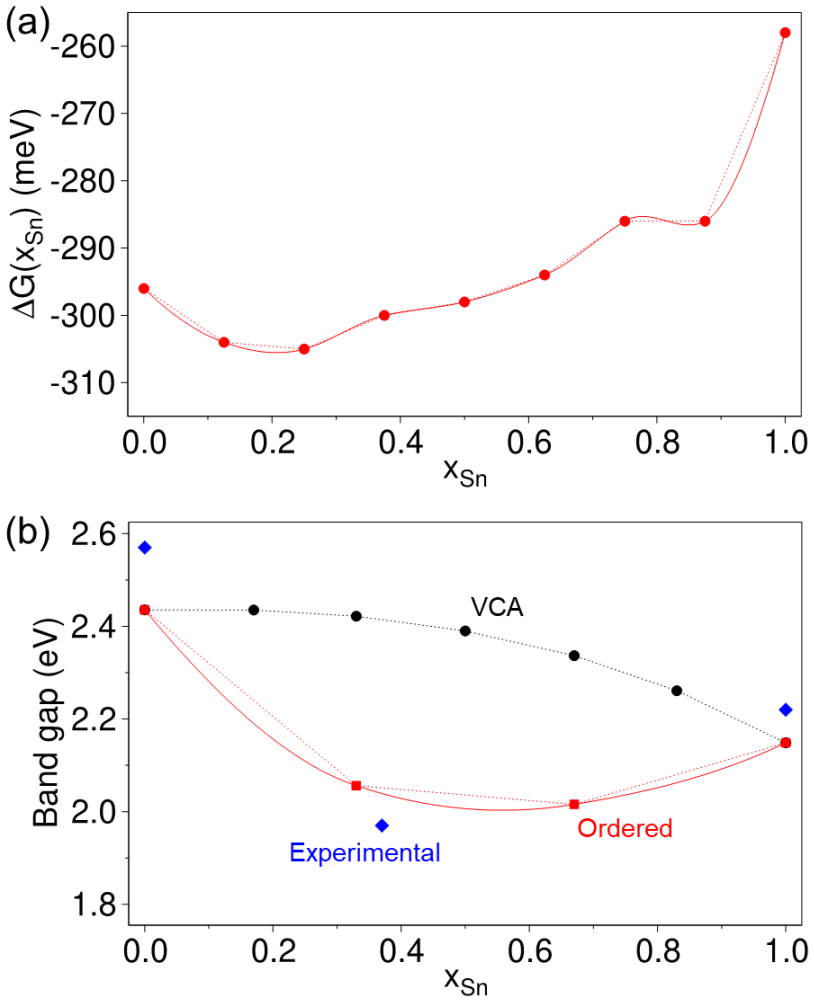

Figure 9. (a) Computed Gibbs free energy of n=1 model systems $Cs_2Pb_{1-x}Sn_xBr_4$ at room temperature. For each value of x, various distributions of Pb and Sn are obtained, only the lowest energies are reported. The plain red line is obtained by interpolation. A global minimum is found around x=0.2 , and a shallow one around x=0.9, indicating a thermodynamic advantage for Pb-rich (and Sn-rich) compounds over the 50:50 alloys. (b) Experimental band gaps of n=3 series $(BA)_2(MA)_2Pb_{3(1-x)}Sn_{3x}Br_{10}$ (blue diamonds). Band gaps of model n=3 systems $Cs_4Pb_{3(1-x)}Sn_{3x}Br_{10}$ calculated using the virtual crystal approximation (VCA, black circles) and supercells containing twelve metallic sites (red squares). Only the lowest energy structures are reported. A rigid shift of 1.2 eV has been applied to the calculated band gaps. The VCA description shows a continuous decrease of the bandgap going from pure Pb to pure Sn structures, whereas the ordered structures exhibit the band bowing experimentally observed and also described in 3D mixed-metal halide perovskites.

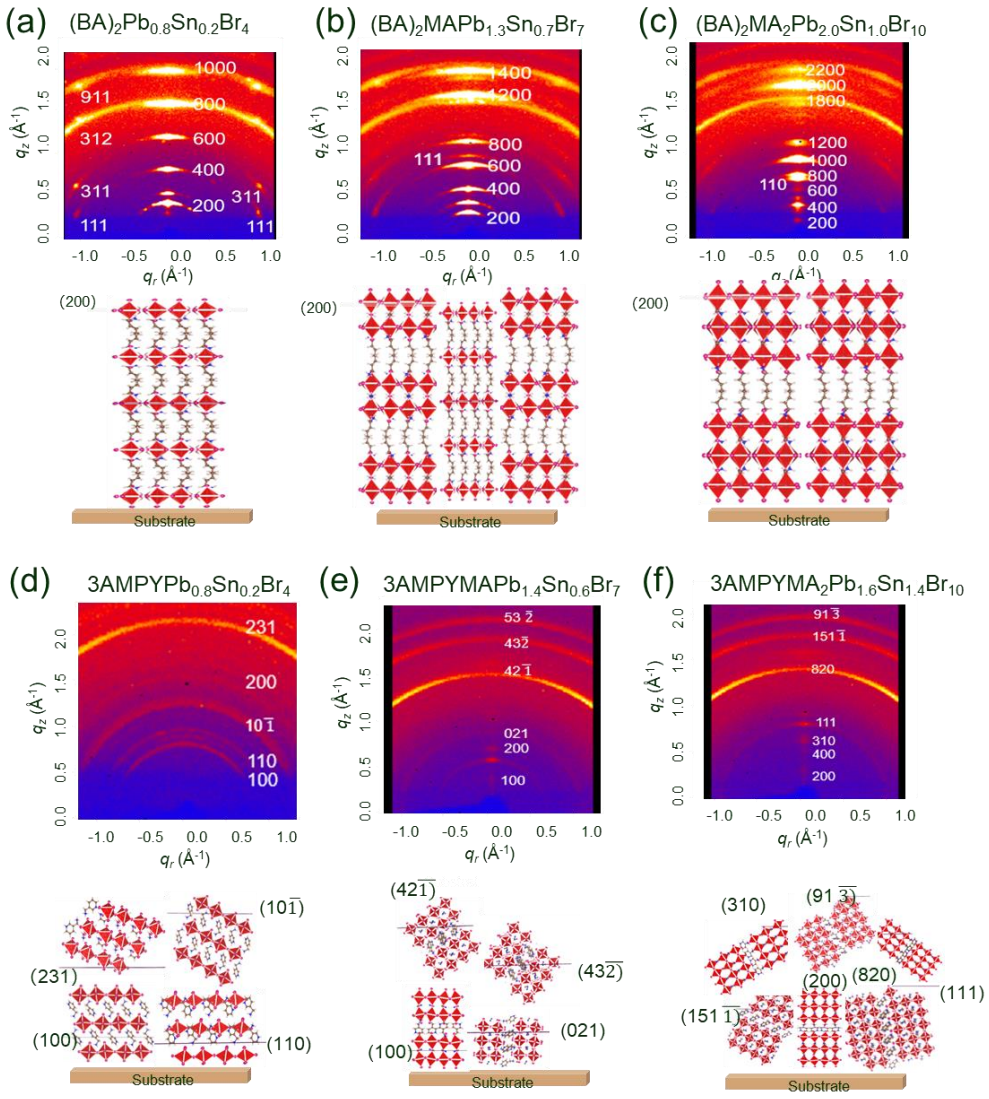

Figure 10. Synchrotron GIWAXS patterns and different thin-film growth orientations of (a-c) $(BA)_2(MA)_{n-1}Pb_xSn_{n-x}Br_{3n+1}$ and (d-f) $(3AMPY)(MA)_{n-1}Pb_xSn_{n-x}Br_{3n+1}$ (n = 1-3) series compounds, respectively. The (h00) planes show in-plane orientation- and (0hh) planes have out-of-plane orientation with peaks labeled.

TOC Graphic

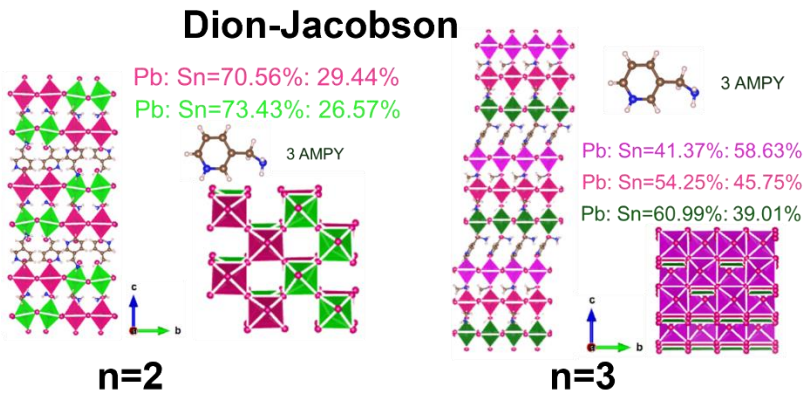
Dion-Jacobson
Pb: Sn=70.56%: 29.44%
Pb: Sn=73.43%: 26.57%
3 AMPY
n=2
3 AMPY
Pb: Sn=41.37%: 58.63%
Pb: Sn=54.25%: 45.75%
Pb: Sn=60.99%: 39.01%
n=3